Construction and Building Materials 283 (2021) 122694

Contents lists available at ScienceDirect

Construction and Building Materials

journal homepage: www.elsevier.com/locate/conbuildmat

Loading rate effects on the properties of fiber-matrix zone surrounding steel fibers and cement based matrix

Van Phi Dang [a], Huy Viet Le [a,b], Dong Joo Kim [a,*]

[a] Department of Civil and Environmental Engineering, SEJONG University, 98 Gunja-dong, Gwangjin-gu, Seoul 143-747, Republic of Korea
[b] Department of Civil Engineering, Hanoi University of Mining and Geology, Hanoi, Viet Nam

HIGHLIGHTS

- MU with higher strength generated the highest loading rate sensitivity of FMZ.
- UHD C-S-H generated higher loading rate sensitivity than HD and LD C-S-H.
- C-S-H with higher calcium to silica (Ca/Si) ratio generated higher loading rate sensitivity.

ARTICLE INFO

Article history:
Received 20 November 2020
Received in revised form 22 January 2021
Accepted 11 February 2021

Keywords:
Loading rate
Nanoindentation
Fiber-matrix zone
Hardness
Young's modulus

ABSTRACT

This study investigated the loading rate effects on the properties of fiber–matrix zone (FMZ) surrounding steel fibers by conducting nanoindentation tests. Ultra-high performance concrete (MU) produced the highest loading rate sensitivity (n) owing to the highest pressure hardening sensitivity of MU although both hardness (H) and Young's modulus (E) of FMZ of other two matrices also clearly increased as loading rate increased from 1 to 8 mN/s. The higher n of MU would be based on the higher content of ultra-high density calcium silicate hydrate. The C-S-H with higher calcium to silica ratio generated higher rate sensitivity.

1. Introduction

High performance fiber reinforced cementitious composites (HPFRCCs) have demonstrated superior mechanical resistance, i.e., higher cracking resistance, strength, ductility, and toughness [1,2]. Moreover, their resistances under earthquakes, impacts, and blasts were significantly higher than those under static rate because their tensile strength and energy absorption capacity were favorably sensitive to strain rate [3–11]. Their enhanced resistance was obtained based on the favorable rate sensitive response of them, employing a lower water to binder ratio and modified binders, with higher homogeneity and less internal micro-cracks [12]. The rate sensitive response of HPFRCCs originated from the rate sensitive interfacial bond strength of steel fibers embedded in cement based matrix, generally determined by conducting single pullout tests or multifiber pullout tests [8,10,11,13–16].

Several researchers have investigated the loading rate effects on the interfacial bond strength of steel fibers by increasing the speed of fiber pullout. Gokoz and Naaman [7] reported that deformed steel fibers in normal strength mortar were highly sensitive to the applied loading speed whereas smooth steel fibers were not. Kim et al. [8] investigated the loading rate effects on the pullout resistance (i.e., interfacial bond strength) of deformed steel fibers by increasing the speed of fiber pullout from static (0.008 mm/s) to seismic rate (18 mm/s): twisted steel fiber was more sensitive to the pullout rate than hooked steel fiber embedded in high strength mortar. Tai and El-Tawil [9] reported that smooth steel fibers were also highly sensitive to the speed of fiber pullouts if

Abbreviations: CH, calcium hydroxide; C-S-H, calcium silicate hydrate; DIF, dynamic increase factor; E, Young's modulus; EDS, energy-dispersive X-ray spectroscopy; H, hardness; HD C-S-H, high density calcium silicate hydrate; HPFRCC, high performance fiber reinforced cementitious composite; FMZ, fiber-matrix zone; ITZ, interfacial transition zone; LD C-S-H, low density calcium silicate hydrate; MH, high-strength mortar; MS, ultra-high performance concrete with a shrinkage-reducing agent; MU, ultra-high performance concrete; n, strain rate sensitivity; NI, nanoindentation; SEM, scanning electron microscopic; UHD C-S-H, ultra-high density calcium silicate hydrate.

* Corresponding author.
E-mail address: djkim75@sejong.ac.kr (D.J. Kim).

https://doi.org/10.1016/j.conbuildmat.2021.122694
0950-0618/

they were embedded in ultra-high performance fiber reinforced concrete (UHPFRC). Park et al. [10,11] found that the amount of UHPFRC matrix shrinkage made significant effects on the pullout resistance and pullout rate sensitivity of smooth steel fibers. It is now well known that the pullout resistance of steel fibers is highly sensitive to the loading rate. However, the source of rate sensitive interfacial bond strength has not been fully understood yet.

The bond strength of steel fibers embedded in cement based matrix is much influenced by the properties of fiber–matrix zone (FMZ) surrounding steel fibers because the mechanical property or resistance of FMZ is generally lower than that of matrix owing to higher porosity at the interfacial transition zone (ITZ) between fiber and matrix [16]. In this study, we investigated the loading rate effects on the properties of the FMZ including ITZ by conducting nanoindentation (NI) tests, scanning electron microscopic (SEM), and energy-dispersive X-ray spectroscopy (EDS) analyses in order to further understand the effects of loading rate on the behavior of HPFRCCs. Deeper understanding about the source of rate sensitive bond strength of steel fibers would be favorable for the development of high performance construction materials with higher strength and energy absorption capacity, especially under high loading rates.

The purpose of this study is to develop further understanding about the source of rate dependent tensile response of HPFRCCs and UHPFRCs by investigating the high rate effects on the properties of FMZ. The specific objectives are to (1) investigate the effect of loading rates of nano-indenter on the FMZ properties of different matrices, (2) compare the rate sensitivity of the FMZ properties corresponding to different matrices and microstructures, and (3) understand the source of rate sensitivity.

2. Background

2.1. ITZ characteristics

The microstructure of ITZ between matrix and fiber plays an important role in the mechanical resistance of HPFRCCs [13,14,16,17]. Both direct and indirect measurement methods have been applied to analyze the chemical compositions and mechanical characteristics of HPFRCCs [18–23]. Indirect measurement methods include various experimental techniques SEM [18,19], Transmission Electron Microscopy (TEM) [20], Electron Backscattered Diffraction (EBSD) [21,22], X-ray Diffraction (XRD) [20,23], and EDS [21], generally used for investigating the microstructure of cement based matrix. One of the direct measurement methods is the NI test, which is used to analyze the mechanical properties of materials at the nanoscale. The applications of the above mentioned methods have revealed the chemical composition and microstructural properties in the ITZ.

The thickness of ITZ was different according to the microstructural characteristics of aggregate particles and the degree of hydration [21], water to cement ratio [24], the types of fibers [17]. The thickness of the ITZ surrounding a steel fiber embedded in high strength mortar matrix was mostly less than 70 μm [17,25]. The width of interfacial cracks at the ITZ between coarse aggregate and cement matrix significantly was also significantly influenced by the properties of concrete [26,27]. Thus, the FMZ within 70 μm distance from the surface of steel fiber was investigated in this study because the thickness of the ITZ was different corresponding to the composition of matrix and less than 70 μm. Kang et al. [13] reported that a higher local stiffness of ITZ by using finer sand grains because the density of calcium silicate hydrate (C-S-H) increased. The high density calcium silicate hydrate (HD C-S-H) and low density calcium silicate hydrate (LD C-S-H) were mainly contained in the hydration products of ordinary concrete as well as in the ITZ of high performance concretes [17,28–30]. Xu et al. [17] mentioned that the main microstructure of the ITZ between steel fiber and the UHPC matrix would be the HD C-S-H. Sorelli et al. [31] reported no weak fiber–matrix ITZ in UHPC due to the predominant presence of the HD C-S-H based on the results of NI tests on the ITZ between steel fiber and UHPC matrix. Zhao and Sun [29] and Vandamme et al. [30] recently reported that the hydration products of cement pates as well as of ITZ mainly contained LD C-S-H, HD C-S-H, and ultra-high density calcium silicate hydrate (UHD C-S-H). A large amount of the HD C-S-H and UHD C-S-H were presented in the UHPC, creating higher mechanical properties of the UHPC than those of ordinary concrete [27,28].

There is little study on the influence of loading rate (or strain rate) on mechanical behavior of cement composites by using NI tests. Most researchers have conducted on other materials such as brittle longmaxi shale (rock) [32], glass [33], sapphire [34], and metal [35,36]. Shi et al. [32] reported that the material behavior of rock was dependent on the loading rate at the nanoscale, as the loading rate increased, the *H*, *E*, yield stress, and indentation shear stress gradually increased. Li et al. [33] indicated that *E* and *H* of the aluminosilicate glass increased linearly with increasing in the loading rates. Bhattacharya et al. [34] also reported that the *H* of sapphire enhanced significantly as the loading rates increased. Furthermore, Vinh et al. [36] stated that *H* and yield strength of structural steel weld zone increased as the strain rate increased. However, Burgess et al. [35] discovered that the hardness, elastic modulus, and deformation energy of metallic glass were independent of the loading rates.

2.2. Nanoindentation tests

Fig. 1a shows a typical nanoindentation load–displacement curve and relevant parameters. As the NI test begins, the load increases gradually to a maximum load (P_{max}) and the penetration depth (h_1). The penetration displacement does not cease as the load holds at P_{max}, but increases to a maximum depth (h_{max}). After unloading process, the indenter tip generally can not return to the original position because of the deformation of material around the indenter and stops at a residual depth which is called final penetration depth (h_p). An effective contact depth (h_c) is used to determine the contact area (A_c), as shown in Fig. 1a. The presence of h_p after the NI test was completed, this indicated that a plastic zone occurred under the indenter [37].

Fig. 1b shows an individual feature of NI tests. The material around the contact area tends to deform upwards or downwards around the indenter tip where the load is applied. This behavior results in pile-up and sink-in of material at the contact boundary [38].

The *H* and *E* are calculated by using the Oliver-Pharr method [39], as provided in Eqs. (1) and (2).

$$H = \frac{P_{max}}{A_c} \tag{1}$$

$$E = (1-\upsilon^2)\left(\frac{1}{E_r} - \frac{1-\upsilon_i^2}{E_i}\right)^{-1} \tag{2}$$

where P_{max} is the maximum load, A_c is the contact area, and υ is the Poisson's ratio of the test samples. υ_i and E_i are poisson's ratio and Young's modulus of the diamond indenter tip, respectively: υ_i is 0.07 and E_i is 1140 GPa for the Berkovich indenter. E_r is the reduced modulus, which can be calculated by using the following Eq. (3).

$$E_r = \frac{\sqrt{\pi}S}{2\beta\sqrt{A_c}} \tag{3}$$

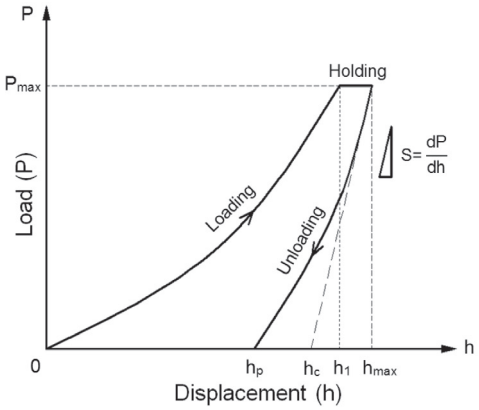

(a) A load-displacement curve

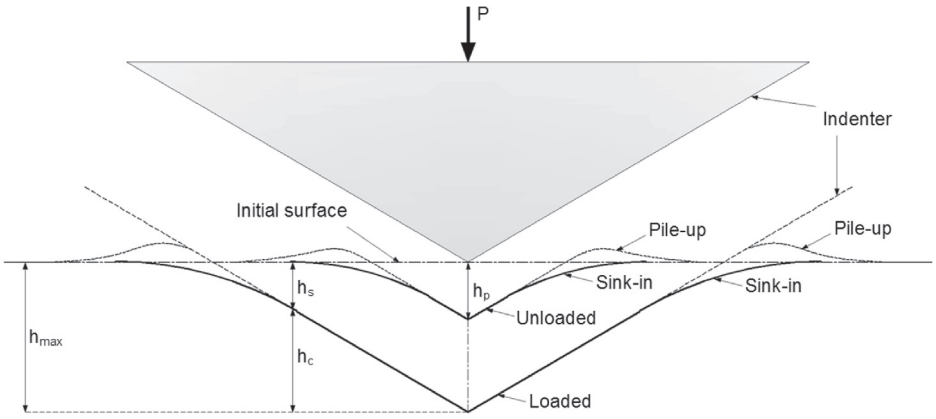

(b) A schematic representation at different indentation status

Fig. 1. Typical nanoindentation test.

where β is a constant depending on the indenter geometry (1.034 for a Berkovich indenter). S is the contact stiffness, which can be determined by the slope of the initial part of unloading curve at the h_{max}, as given by Eq. (4)

$$S = \left(\frac{dP}{dh}\right)_{h = h_{max}} \tag{4}$$

Strain rate sensitivity (n) is used to evaluate the effect of strain rate on material properties [32,40–45]. The n is calculated by using the following Eqs. (5) and (6):

$$n = \frac{\partial Log(H)}{\partial Log(\dot{\varepsilon})} \tag{5}$$

$$\dot{\varepsilon} = \frac{1}{2}\frac{\dot{P}}{P_{max}} \tag{6}$$

The following Eq. (7) can be obtained by integrating Eq. (5) [32]:

$$Log(H) = nLog(\dot{\varepsilon}) + Log(H_0) \tag{7}$$

where $\dot{\varepsilon}$ is strain rate corresponding to the loading rate ($\dot{P}$) of 1 and 8 mN/s would be calculated as 0.05 and 0.4 s^{-1}, respectively because the P_{max} in this study was 10 mN. H_0 is the intrinsic hardness free from strain rate sensitivity. Both n and H_0 were generally determined by fitting the curve of Log(H) and $Log(\dot{\varepsilon})$ [32,44].

Besides, a dynamic increase factor (DIF) of E and H is also used to assess the loading rate sensitivity of the material. The DIF in the following Eq. (8) is a dimensionless number that expresses the change of the material response when the loading or strain rate changes. In this study, both the n and the DIF were used to estimate the effect of strain rate on material properties.

$$DIF = \frac{\Delta_i}{\Delta_j} \tag{8}$$

where Δ_i and Δ_j are the material response at high and low loading rates, respectively.

3. Experiments

Fig. 2 illustrates an experimental program to investigate the source of rate sensitive responses of the FMZ. The high-strength smooth steel fibers and three matrices were used to investigate the source of rate sensitivity of the FMZ. The three matrices were ultra-high performance concrete (MU), MU with a shrinkage-reducing agent (MS), and high strength mortar (MH).

3.1. Materials and specimen preparation

Table 1 provides the properties of the compositions and compressive strength at the age of 14 days of the MU, MS, and MH matrices while Table 2 does the properties of brass coated high strength smooth steel fibers.

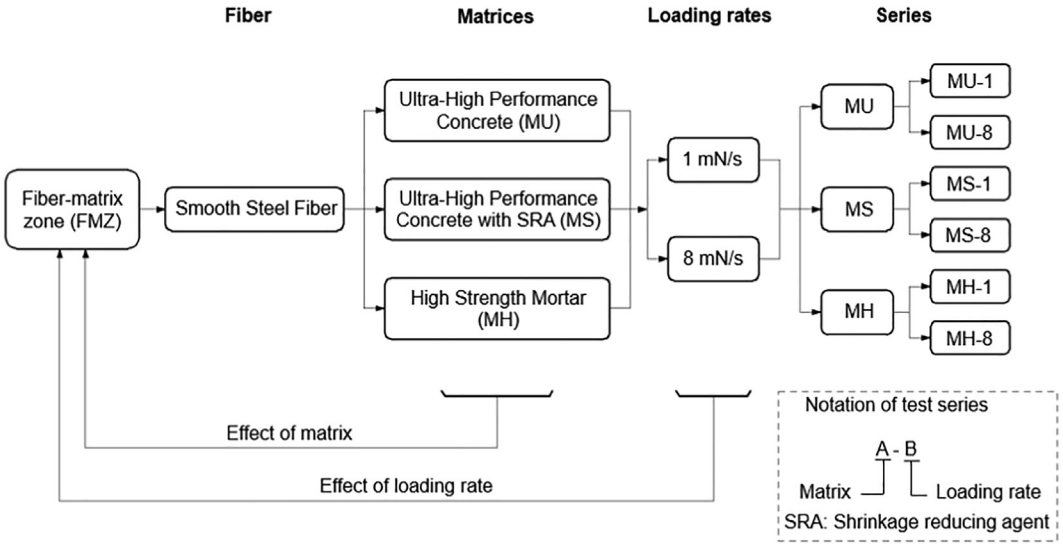

Fig. 2. Experimental program.

Table 1
The composition and compressive strength of matrices.

Matrix type	Cement (type)	Silica sand		Fly ash	Silica fume	Silica powder	Superplasticizer		Shrinkage reducing agent	Water/binder ratio	Compressive strength (MPa)
		A	B				C	D			
MU	1.00 (I)	1.10		–	0.25	0.30	0.067		–	0.17	187
MS	1.00 (I)	1.10		–	0.25	0.30	0.067		0.01	0.18	170
MH	1.00 (III)		1.10	0.15	–	–		0.009	–	0.31	98

A and *B* are grain size of approximately 210–250 μm and 300–700 μm, respectively.
C and *D* are superplasticizer provided by solid contents of 30% and 25%, respectively.

Table 2
Properties of straight smooth steel fibers.

Diameter (mm)	Length (mm)	Density (g/cm^3)	Tensile strength (MPa)	Elastic modulus (GPa)	Material
0.2	19	7.9	2788	200	Brass coated high strength steel fibers

Type I cement was used in both MU and MS whereas Type III cement was used in MH. The grain size of silica sand used in both MU and MS varied between 210 and 250 μm, whereas that used in MH did between 300 and 700 μm. Both MU and MS matrix utilized polycarboxylate ether superplasticizer with solid contents of 30%, whereas MH did that with solid contents of 25%. Shrinkage reducing agent (SRA) based on propylene-glycol ether with a density of 3.18 g/m^3 was used in MS. Silica fume contains approximately 98.5% SiO_2 and its grain size ranges from 0.1 to 1.0 μm. Silica powder with an average grain size of 10 μm used as a filler in matrix. The composition of silica powder is 98.0% SiO_2 and its density is 2.6 g/m^3.

A total of three samples were prepared for nano experiments corresponding to MU, MS, and MH matrix. The procedure of sample preparation includes six steps as follows:

(1) Mixing: the mortar matrices were prepared by using a Hobart-type mixer with 20 L capacity. Cement, silica sand, silica fume, and silica powder were firstly dry-mixed for 10 min. After dry mixing, water was gradually added while the mixture was mixed for 3 min, then the superplasticizer was added, and then the mortar mixture was further mixed for 3 min.

(2) Casting: Fig. 3a shows the geometry of a mold with two-parts used to cast the specimens. Nine steel fibers were fixed in the middle of a mold by using a foam sheet prior to casting, as shown in Fig. 3b. Then, the mortar mixture was poured into the mold with slight vibration for 2 min.

(3) Curing: all the samples were covered by plastic molds and stored at laboratory (20 ± 2 °C) after casting for two days prior to demolding. The specimens of MU and MS were cured in a hot water tank (90 ± 2 °C) for three days while those of MH with Type III cement were cured in a water tank for 14 days at the temperature of 20 ± 2 °C in a laboratory.

(4) Cutting: all the specimens were under dry condition for 14 days after curing and then were sliced into a square with dimension of 20 × 20 mm^2 and put into the middle of the mounting cup with a diameter of 31 mm as shown in Fig. 3. The mixture of epoxyset with the resin to hardener ratio of 100:12 by weight was prepared. Then, the mixture was poured into the mounting cup and then cured for eight hours in the vacuum impregnation system (VacuPrep™) to maintain sample integrity during abrasive preparation by reducing the chance of cracking or delamination.

(5) Grinding and polishing: a grinding and polishing machine (MetPrep4/PH-4™) was used. Table 3 provides the procedure of grinding and polishing in detail. At each step of grinding process, tap water was added for a short time to remove any matrix debris attached to sample holder and abrasive papers. Further grinding was done with polishing cloth containing 3 μm diamond suspension and 0.04 μm colloidal silica suspension, respectively. A Pur-

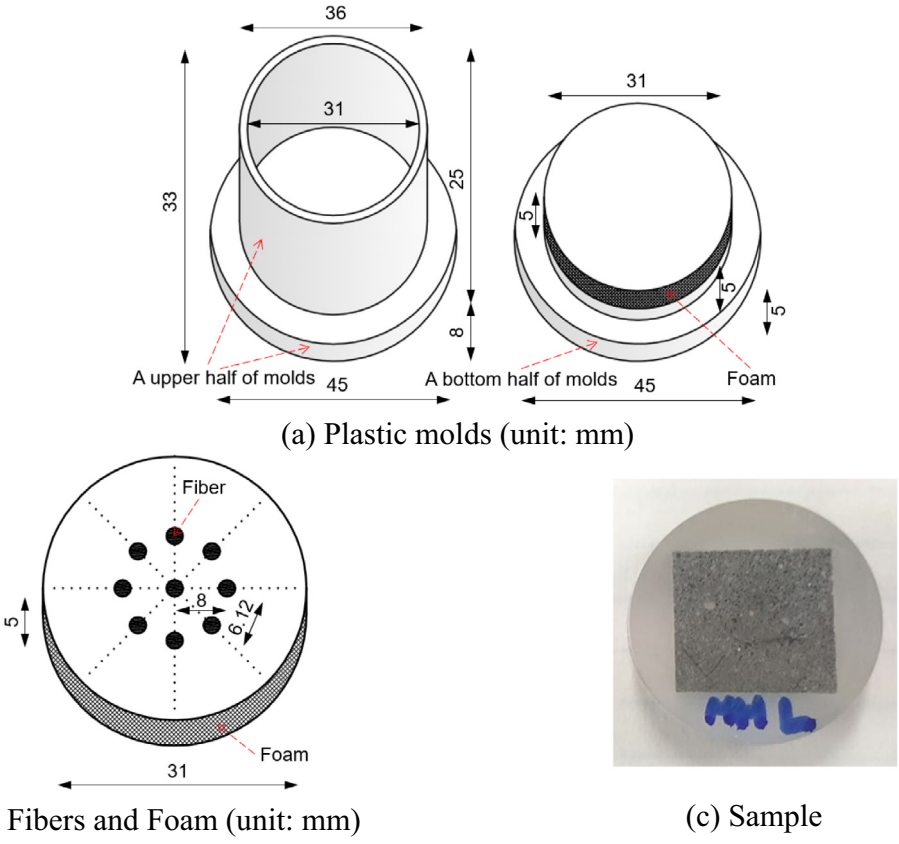

Fig. 3. Images of molds and sample.

Table 3
Steps of grinding and polishing samples.

Step	Grinding				Polishing	
	1	2	3	4	5	6
Abrasive	400 Grit (P–800)	600 Grit (P–1200)	800 Grit (P–2400)	1200 Grit (P–2400)	3 μm	0.04 μm
Type	SiC	SiC	SiC	SiC	Diamond	Colloidal Silica
Carrier	Abrasive Disc	Abrasive Disc	Abrasive Disc	Abrasive Disc	Suspension	Suspension
Polishing Cloth					DiaMat	Chem–Pol
Coolant	Water	Water	Water	Water	PurpleLube	–
Platen Speed (RPM) Direction	150/Comp	150/Comp	150/Comp	150/Comp	150/Comp	100/Contra
Sample Speed (RPM)	120	120	120	120	110	90
Force (lbF)	4	4	4	4	4	4
Time (min)	Until Flat	2	3	3.5	3	30

pleLube, water-free alcohol based lubricants, was then used to enhance the polishing performance of diamond suspension and colloidal silica suspension. The sizes of each sample are a diameter of 31 mm and height of 10 mm.

(6) Roughness checking: a typical sample for a NI test is shown in Fig. 3c. The surface roughness of the samples was measured by using an atomic force microscope (XE-100 Park systems). The root mean square roughness number (RMS) was calculated by using Eq. (9) [46]:

$$RMS = \sqrt{\frac{1}{n.m}\sum_{i=1}^{n}\sum_{j=1}^{m}(h_{ij} - h_{mean})^2} \quad (9)$$

where n, m denote the pixel size of the atomic force microscope (AFM) image, h_{ij} is the height reading in pixel (i, j) and h_{mean} is the mean value of all height readings in the image.

The average values of surface roughness (28.90, 25.95, and 73.20 nm) in the FMZ of MU, MS, and MH matrix were within the allowable limitation for the NI tests with a Berkovich tip [17,47,48]. All the samples were kept in a vacuum container to prevent or minimize any further hydration prior to testing.

3.2. Test method and procedures

Fig. 4 shows a setup for a NI test. Fig. 4a presents two positions where NI tests were carried out corresponding to two loading rates of 1 and 8 mN/s. To investigate the effect of loading rate on the properties of FMZ including ITZ corresponding to MU, MS, and MH matrix, NI tests were carried out in two zones in the FMZ surrounding a steel fiber, each zone contained 40 indented points, and thus 80 indented points per a steel fiber were indented as shown in Fig. 4a. Since a sample contains nine steel fibers, thus a total of 720 points were indented corresponding to three different matrix.

Fig. 4b shows the detail of each indented point location. The distance between each line in an area was set as 10 μm along the Y-axis for all samples. Note that for each row along the X-axis, there

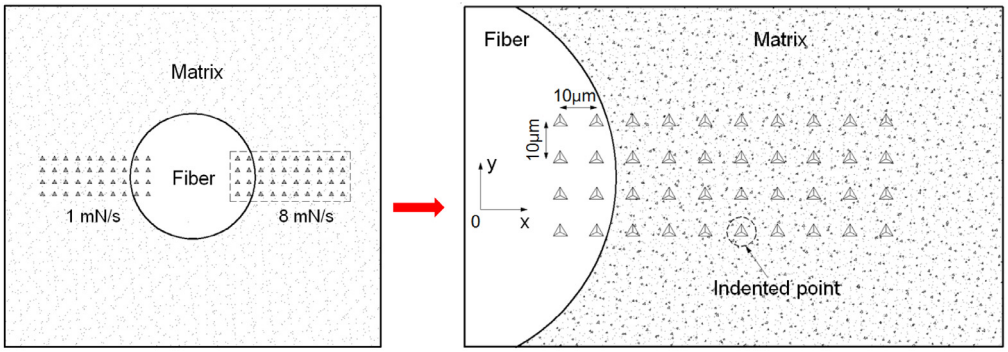

(a) Indentation points arrangement (b) A grid of indentation points

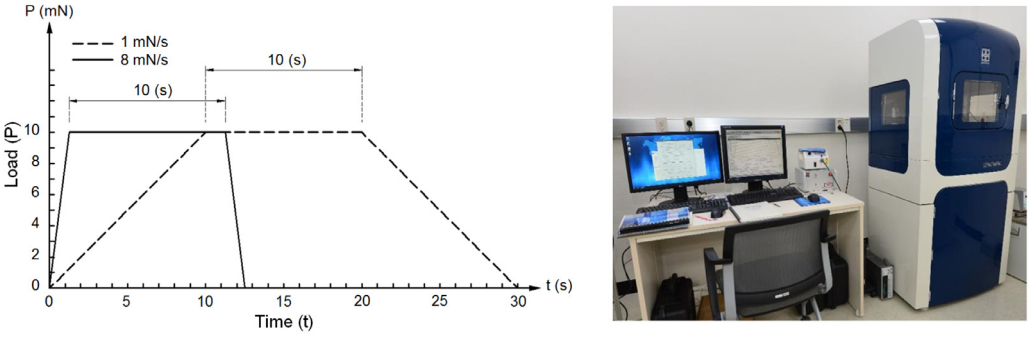

(c) Indentation load versus time curves (d) A TI950 Triboindenter system

Fig. 4. A setup for a nanoindentation test and a nanoindentation system.

were 10 indented points, in which two indented points located in the section of steel fiber to find the indented points after completed NI test (Fig. 4b). The spacing of indented points was 10 μm to avoid any interaction between two adjacent indents [31].

Fig. 4c compares two indentation load versus time curves corresponding to the loading rates 1 and 8 mN/s. The indentation load linearly increased from zero to the maximum indentation load of 10 mN, then it was held constant for 10 s prior to unloading process, as shown in Fig. 4c.

Fig. 4d shows a TI950 Triboindenter system with a three-sided Berkovich diamond tip that was used to investigate the property of FMZ of the MU, MS, and MH, respectively. The TI950 Triboindenter has a load range from 30 nN to 10 mN, the resolution of load and displacement was less than 1 nN and 0.04 nm, respectively.

4. Results and discussion

4.1. Loading rate effects on P-h curves of FMZ

Fig. 5 shows typical P-h curves of different microstructures of FMZ of matrices corresponding to the loading rates of 1 and 8 mN/s. The microstructures, in Fig. 5, at the position of indented points within the investigated FMZs were determined based on the result of EDS tests.

The P-h curves of microstructures including sand, clinker, C-S-H, and CH (Fig. 5a and b) was generally similar to the typical curve in Fig. 1a. However, the P-h curve of the porosity in FMZs was clearly different, especially at the initial part, as can be seen in Fig. 5c and d. Besides, the nanoindentation depth of the porosity was significantly higher than that of other microstructures owing to very low hardness of the porosity.

Fig. 6 illustrates the SEM images in the FMZ between steel fiber and mortar matrix. The position of the indented points in the FMZ is well-matched with the grid of indentation points in Fig. 4b. Furthermore, Fig. 6b and c show typical sink-in of indented points after NI tests corresponding to the loading rate of 1 and 8 mN/s, respectively. The side length of the projected indentation area is 1.73 μm, at the loading rate of 1 mN/s, higher than that (0.92 μm) at the loading rate of 8 mN/s. Xu et al. [37] also reported that the side length of the projected indentation area decreased as the loading rates increased. A higher side length of an indented point at lower loading rate (1 mN/s) would be due to a higher contact depth (h_c). Therefore, the values of A_c and an edge of a contact area at the loading rate of 8 mN/s was smaller than that of the loading rate of 1 mN/s.

Fig. 7 shows the effects of loading rates on the nanoindentation depths including h_{max}, h_c, and h_p of MU, MS, and MH matrices. As the loading rate increased from 1 to 8 mN/s, the h_{max}, h_c, and h_p clearly decreased. At the loading rate of 1 mN/s, the h_{max} was 597.89 nm for MU, 620.93 nm for MS, and 770.08 nm for MH. However, at the loading rate of 8 mN/s, the h_{max} of MU, MS and MH was 447.80, 525.68, and 706.42 nm, respectively. Furthermore, a smaller h_{max} was always obtained at higher loading rate (8 mN/s) than at lower loading rate (1 mN/s), as shown in Fig. 7.

This tendency is in good agreement with the results reported by Li et al [33] that the h_{max} decreased with the increase of the loading rate. The h_c and h_p of MU at both the loading rates of 1 and 8 mN/s were the lowest ones whereas those of MH were the highest ones. Furthermore, the h_p of MU corresponding to the loading rates of 1 and 8 mN/s was 385.48 and 255.92 nm, respectively, whereas that of MH was 520.77 and 485.11 nm, respectively. As the loading rate increased from 1 to 8 mN/s, the h_c of MU was 537.21 and 381.29 nm whereas that of MH was 707.20 and 644.03 nm. Shi

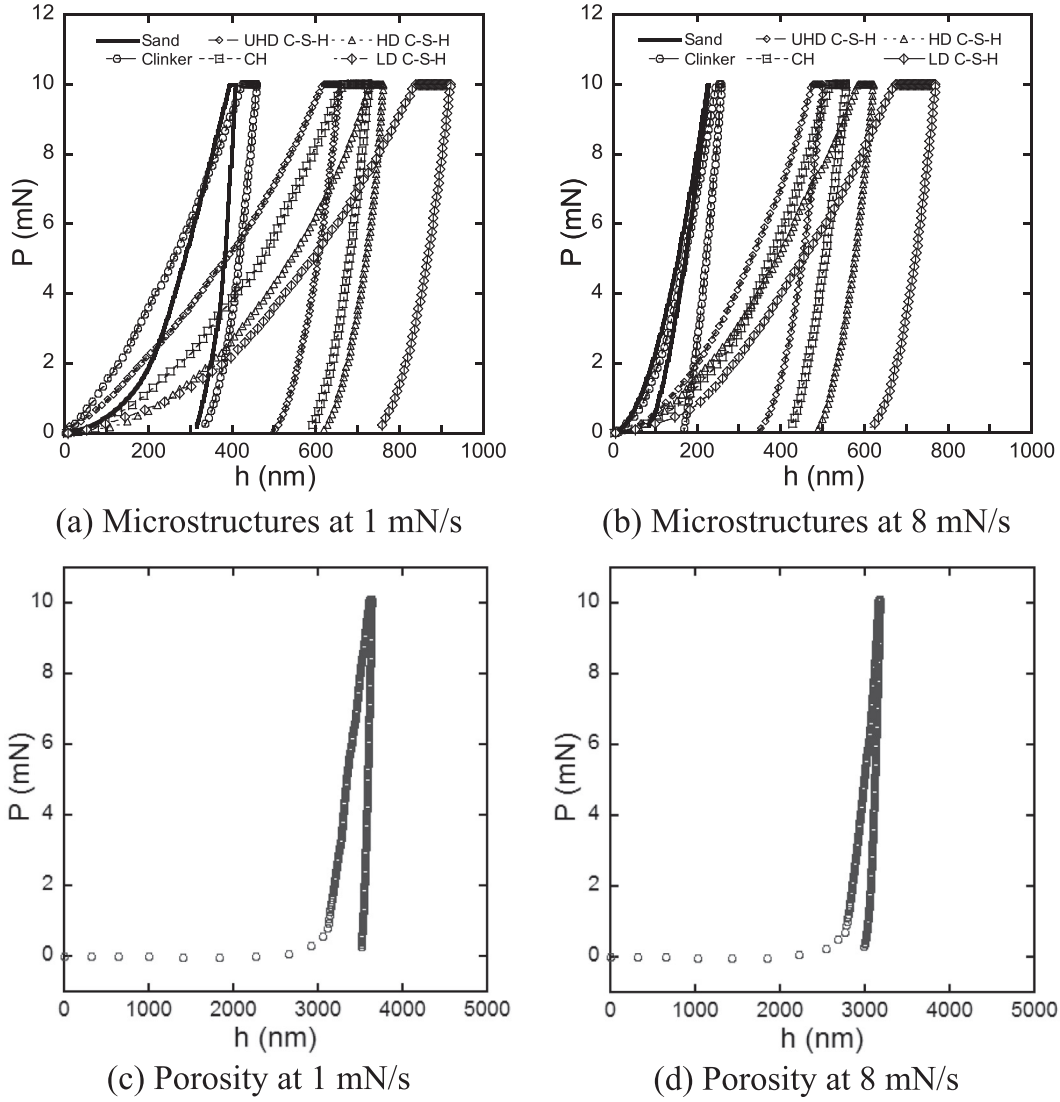

Fig. 5. Typical P-h curves of different microstructures of FMZ.

et al. [32] also reported that the h_p, h_c, and h_{max} decreased as the loading rate increased. A decrease in the h_c clearly caused a decrease of contact area (A_c). The higher loading rate resulted in the lower maximum penetration and contact depth, indicating the lower contact areas at the higher loading rate and consequently increased the *H* value.

In general, as loading rate increased, both *H* and *E* of all matrices increased, as shown in Fig. 8. As the loading rate increased from 1 to 8 mN/s, the average value of *H* of FMZ increased from 2.20 to 3.84 GPa for MU, from 2.14 to 3.20 GPa for MS, and from 1.59 to 2.32 GPa for MH, respectively. Besides, the average value of *E* of MU highly increased from 42.46 to 62.50 GPa while that of MS did from 41.54 to 54.55 GPa, and that of MH did from 37.53 to 40.86 GPa. The loading rate-dependent *H* and *E* of cement based matrices including MU, MS, and MH was found to be similar to the trend of other materials such as rock, zirconia, silicon carbide, and alumina at the nano-microscale [32,44,49–51].

4.2. Comparative rate sensitivities of FMZ properties corresponding to different matrices and microstructures

The matrix with higher compressive strength was found to be more sensitive to the loading rates than the matrices with lower compressive strength. To estimate the rate sensitivity, both *DIFs* (for *H* and *E*) and strain rate sensitivity (*n*) were used. Fig. 9 shows the *DIFs* and *n* of FMZ corresponding to different matrices. As the loading rate increased from 1 to 8 mN/s, the *DIFs* of both *H* and *E* in MU were notably higher than those in MS and MH. The *DIF* for *H* was 1.75, 1.50, and 1.46 corresponding to MU, MS, and MH, respectively while that for *E* was 1.47, 1.31, and 1.09, respectively. As the loading rate increased from 1 to 8mN/s, MU produced the highest strain rate sensitivity (*n*) among the three matrices. The n of MU, MS, and MH was 0.27, 0.19, and 0.18, respectively.

The effect of loading rate on microstructures including LD C-S-H, HD C-S-H, UHD C-S-H, CH, clinker, and sand of the FMZs was also analyzed. The chemical composition and atomic density of the microstructures in FMZ were investigated by using the results of EDS at all the indented points, as shown in Fig. 10. Table 4 provides the atomic density of selected atoms in the indented points corresponding to different microstructures. The chemical composition of CH, clinker, and sand was not much different corresponding to the different (MU, MS, and MH) matrices. However, that of UHD, HD, and LD C-S-H was notably different corresponding to the different matrices. The calcium to silica (Ca/Si) ratio was one of the main parameters for determining the C-S-H [52–55]. The Ca/Si of MU is 2.36 ± 0.31, 1.70 ± 0.24,

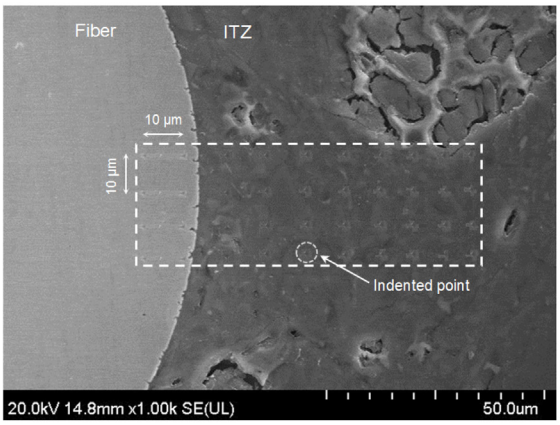

(a) A typical interfacial transition zone between a smooth steel fiber and matrix

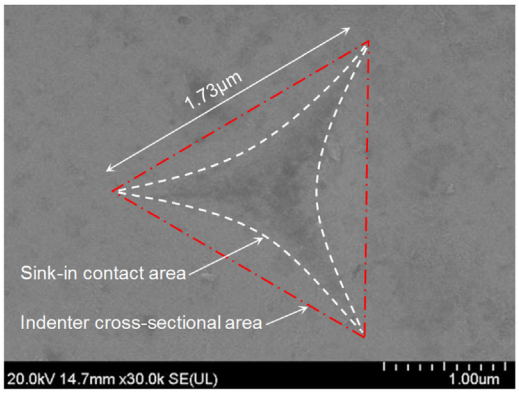

(b) 1 mN/s

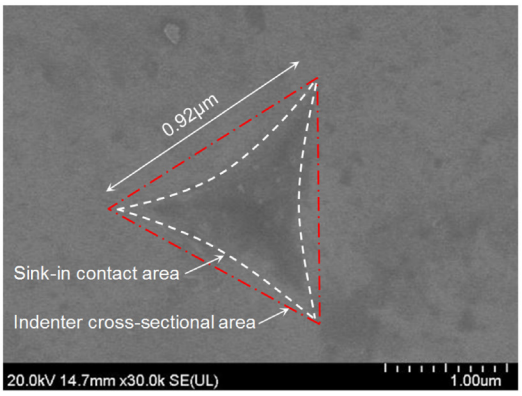

(c) 8 mN/s

Fig. 6. Typical SEM images of the interfacial transition zone and indented points corresponding to loading rates of 1 and 8 mN/s.

and 0.72 ± 0.21 corresponding to the UHD, HD, and LD C-S-H, respectively, while that in MS is 2.25 ± 0.28, 1.58 ± 0.22, and 0.60 ± 0.23, respectively. Furthermore, the Ca/Si of the HD and LD C-S-H in MH matrix is 1.12 ± 0.32 and 0.52 ± 0.19, respectively. The UHD C-S-H was not found in MH matrix while other HD and LD C-S-H were found in all of the matrices. Vandamme et al [30] and Sorelli et al [31] also reported that the UHD and HD C-S-H were contained in UHPC.

After identifying the microstructure, the property, H and E, distribution of the microstructures was determined by using a statistical analysis (deconvolution technique) [17,30,31]. This technique was performed by deconvoluting the experimental distribution values of the mechanical properties x by the sum of k theoretical probability distribution functions p_j. The parameters (f_j, p_j, μ_j, and s_j) were determined by minimizing the difference between the experimental probability density function (PDF) and theoretical PDF, as follows:

$$\min P(x) = \sum_{i=1}^{m} \sum_{x=(H,E)} \left(\sum_{j=1}^{k} f_j p_j\left(x_i, \mu_j, s_j\right) - P(x_i) \right)^2 \quad (10)$$

where m is the number of bins that the problem is discretized, x is the H or E of each microstructure j; f_j is the frequency of each microstructure j; μ_j and s_j are the mean and standard deviation of x of each microstructure j; and p_j is the theoretical probability of the microstructure j, which is assumed by the Gaussian distribution [17,31]:

$$p_j = \frac{b}{\sqrt{2\pi s_j^2}} \exp\left(\frac{-(x-\mu_j)^2}{2s_j^2} \right) \quad (11)$$

where b is the bin size: b = 0.1 GPa if $x = H$ and b = 1.0 GPa if $x = E$. To identify statistically relevant microstructure properties with a sufficient contrast, the overlap of successive Gaussian curves representative of two microstructures is constrained by [17,31]:

$$\mu_j^x + s_j^x < \mu_{j+1}^x + s_{j+1}^x, \; x = (H, E) \quad (12)$$

Fig. 11 shows the PDF curves of hardness of FMZ of MU, MS, and MH at the loading rate of 1 mN/s while Table 5 provides the deconvolution results of the FMZs for all matrices by using deconvolution technique including the volumetric proportion. The C-S-H microstructure, including UHD C-S-H, HD C-S-H, and LD C-S-H, was main ingredients in all three matrices. The percentage of C-S-H in FMZ of MU, MS, and MH was approximately 70%, 67%, and 63%, respectively. MU matrix showed the lowest percentage of porosity of FMZ whereas MH matrix did the highest one, as provided in Table 5. Besides, the percentage of clinker in MU (10.12%) and MS (9.15%) was notably higher than that in MH (7.37%). This would be attributed to the lower water to cement (w/c) ratio of MU and MS. Cement clinker is always residual even long after hydration as the w/c ratio is less than 0.42 [31].

Fig. 12 shows the porosity area in the FMZ of the matrices. The SEM-BSE images were used to calculate the percentage of porosity area according to the distance from fiber until 70 μm, respectively,

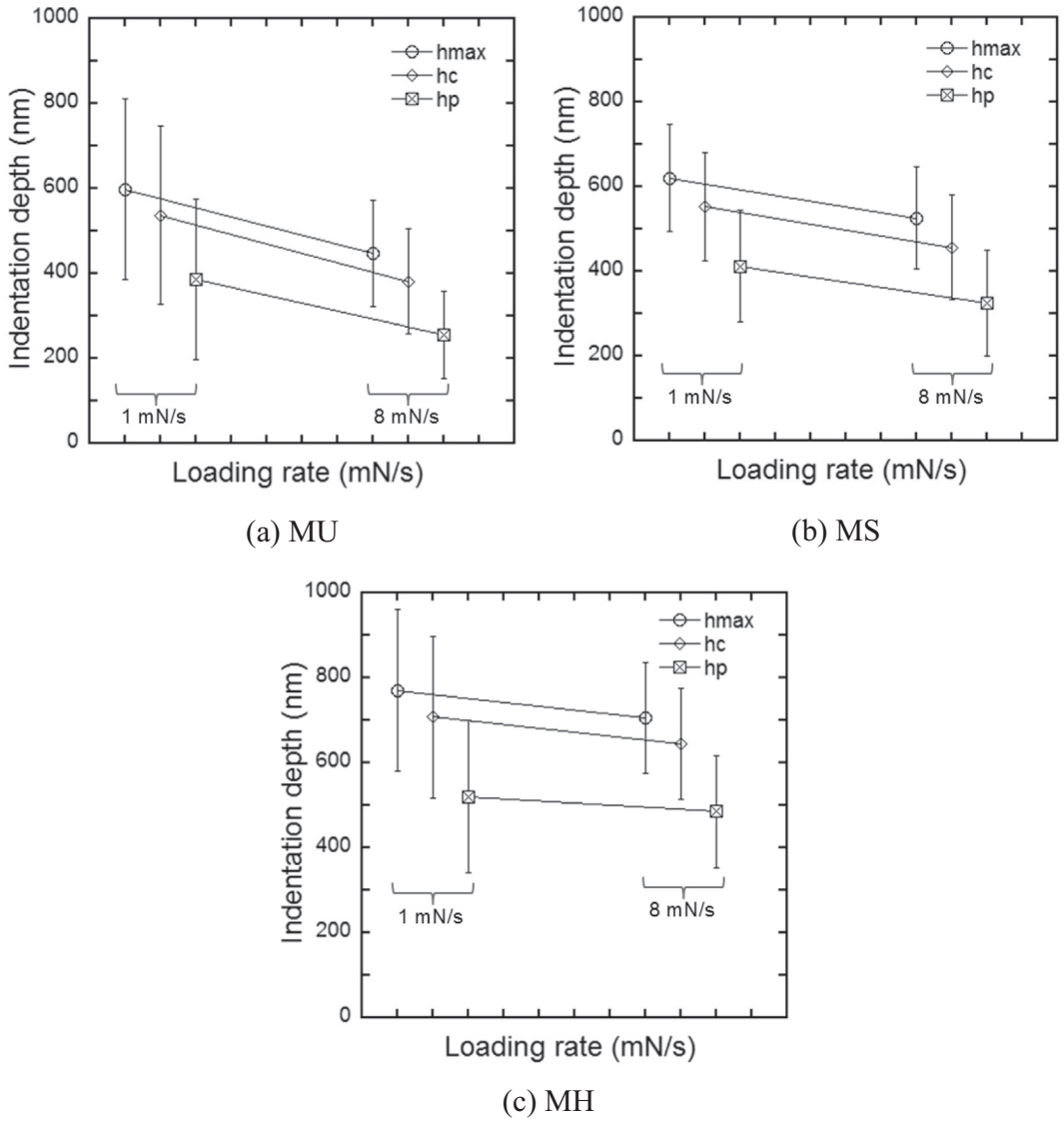

Fig. 7. Effects of loading rates on the nanoindentation depths in FMZ of matrices.

as shown in Fig. 12a. MU matrix produced the lowest porosity in the FMZ surrounding fiber, whereas the MH matrix did the highest one, as shown in Fig. 12b. The porosity area of the first layer with 10 μm from fiber surface was 5.88% and 17.68% corresponding to MU and MH matrix, respectively. This trend is completely consistent with the experimental frequency of porosity of the FMZ based on NI tests, as provided in Table 5. This is attributed to the effects of water to cement (w/c) ratio and shrinkage-reducing agent (SRA). The higher w/c ratio generally produced more porous in the microstructure of cementitious materials.

As the loading rate increased from 1 to 8 mN/s, both *E* and *H* of all microstructures including LD C-S-H, HD C-S-H, UHD C-S-H, CH, clinker, and sand in the FMZs clearly increased, as can be seen in Fig. 13. Thus, the increase in *H* and *E* of FMZs of matrices was attributed to the increase in *H* and *E* of microstructures of FMZs with increasing loading rate.

The viscoelastic nature of C-S-H would be one of main sources for the observed rate sensitive *H* and *E*, and eventually for the rate sensitive interfacial bond resistance of steel fibers. The C-S-H with higher Ca/Si ratio was more sensitive to loading rate. The *DIFs* for *H* and *E*, and strain rate sensitivity (*n*) were clearly different according to the different microstructures, as shown in Fig. 14. The *DIFs* for both *H* and *E*, and *n* of UHD and HD C-S-H were larger than those of LD C-S-H. The *DIFs* for the *H* were varied from 1.54 to 1.56 for UHD C-S-H, from 1.38 to 1.52 for HD C-S-H, and from 1.14 to 1.45 for LD C-S-H, respectively, while that for *E* were between 1.38 and 1.39 for UHD C-S-H, between 1.10 and 1.36 for HD C-S-H, between 1.01 and 1.31 for LD C-S-H, respectively. The n of UHD, HD, and LD C-S-H in MU matrix was 0.21, 0.20, and 0.18, respectively. The Ca/Si ratio of UHD and HD C-S-H in each matrix was higher than that of LD C-S-H, as provided in Table 4. In addition, the Ca/Si ratio of calcium silicate hydrate (C-S-H) in FMZ of MU matrix was is higher than that of MS and MH matrices. The Ca/Si ratio was clearly dependent upon a water to cement (w/c) ratio and matrix composition [53,56]. Thus, to improve the loading rate sensitivity of FMZs, the amount of C-S-H microstructures with higher Ca/Si ratio should be enhanced.

4.3. Source of rate sensitive nanoindentation response

Many researchers have reported that the source of rate sensitive nanoindentation was dependent upon pressure hardening [32,44,57,58]. However, their results were based on the NI tests for metals and rocks except for concrete. Chen [57] firstly proposed

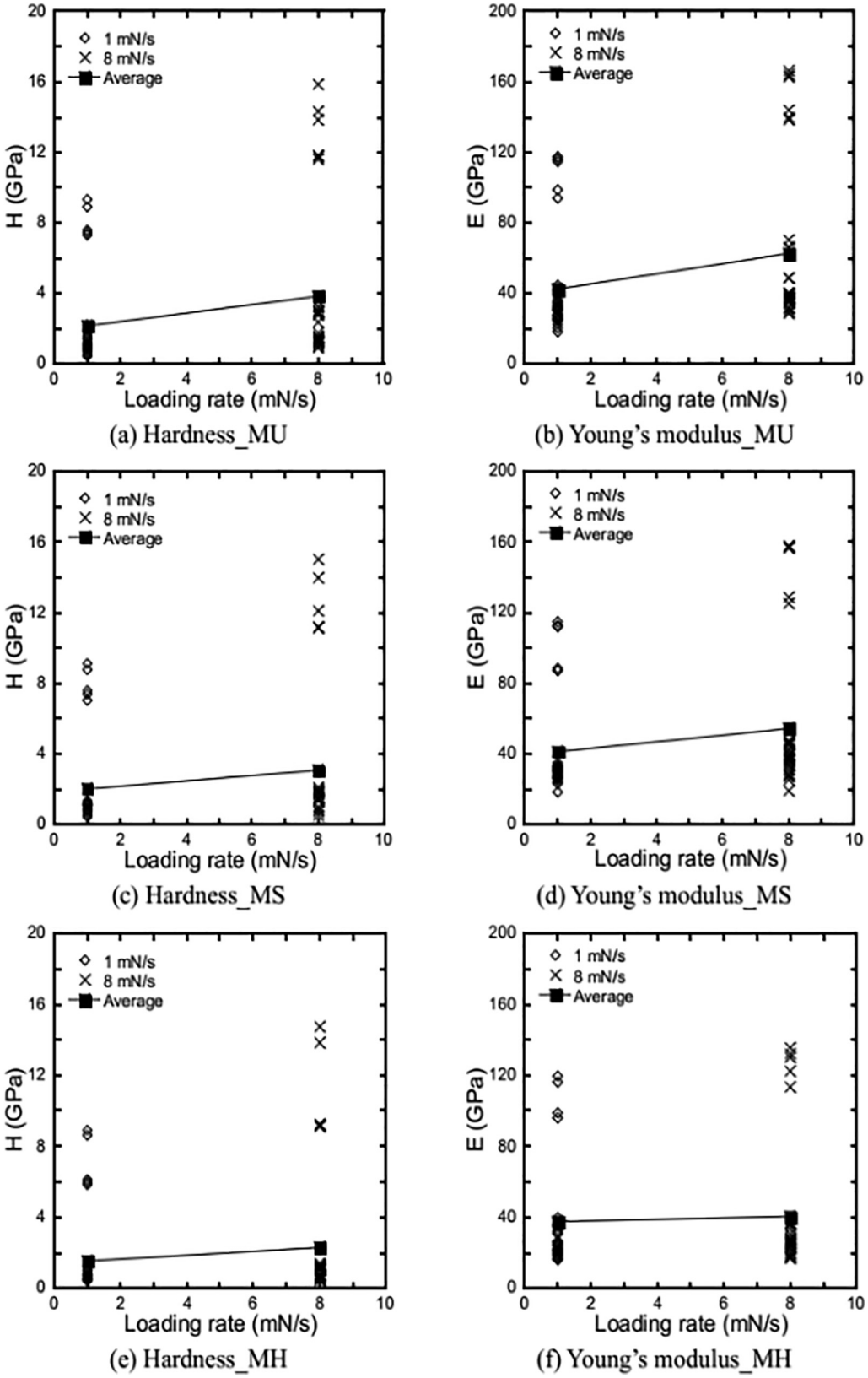

Fig. 8. Loading rate effects on Hardness and Young's modulus of FMZ of matrices.

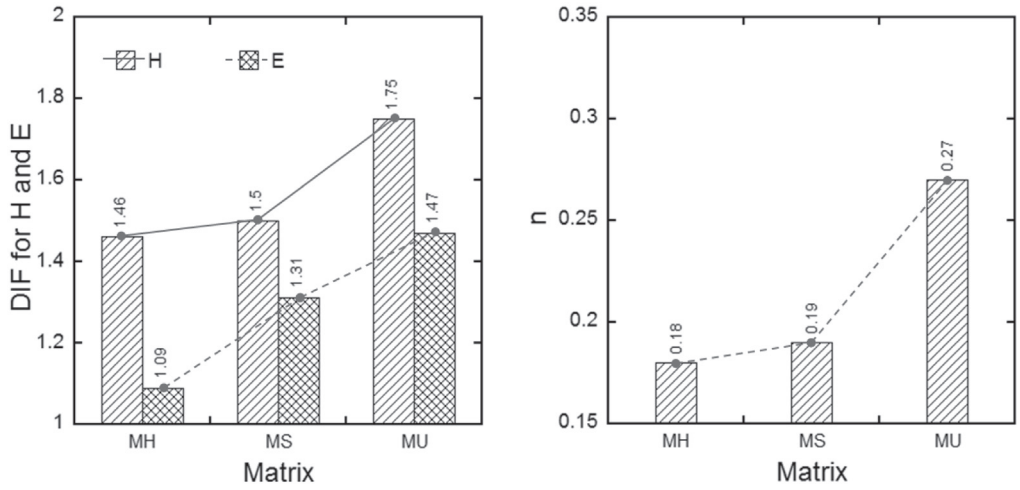

(a) DIFs for H and E (b) *n*

Fig. 9. DIFs and strain rate sensitivity (*n*) of FMZ corresponding to MU, MS, and MH.

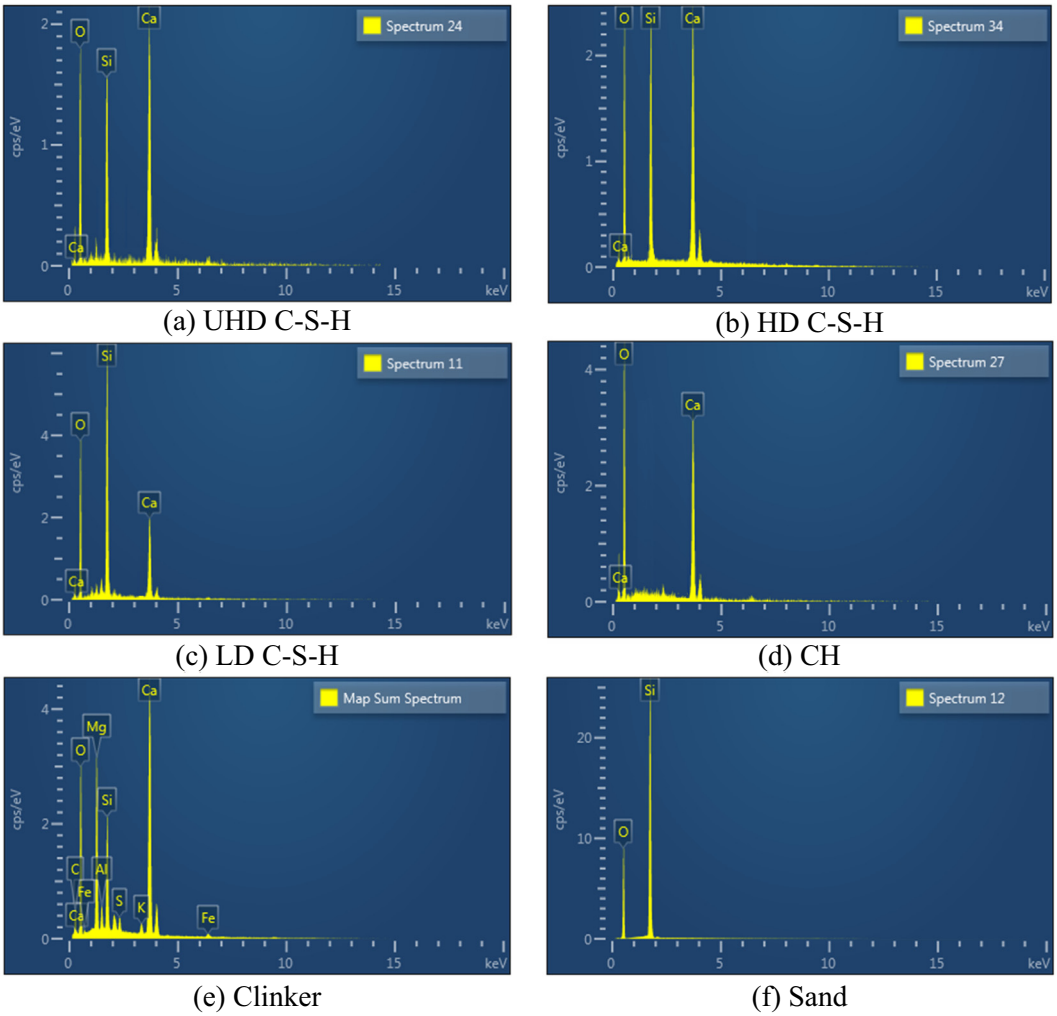

(a) UHD C-S-H (b) HD C-S-H

(c) LD C-S-H (d) CH

(e) Clinker (f) Sand

Fig. 10. Typical results of the different microstructures by using EDS.

Table 4
Typical atomic density of the different microstructures.

Matrix	Phase	Atomic density (%)									Ca/Si
		Ca	Si	O	S	Al	Fe	Mg	K	Na	
MU	UHD C-S-H	21.18	8.97	66.01	0.63	0.76	0.43	0.34	0.82	0.86	2.36 ± 0.31
	HD C-S-H	14.84	8.72	72.57	0.62	0.80	0.41	0.36	0.80	0.88	1.70 ± 0.24
	LD C-S-H	10.07	14.00	71.99	0.64	0.75	0.44	0.38	0.84	0.89	0.72 ± 0.21
	Sand	–	37.01	62.99	–	–	–	–	–	–	–
	Clinker	25.91	4.20	63.21	1.12	1.77	1.52	–	1.25	1.02	6.17 ± 0.26
	CH	17.98	0.92	77.16	0.65	0.79	0.42	0.35	0.81	0.92	–
MS	UHD C-S-H	19.30	8.57	68.28	0.59	0.80	0.45	0.36	0.79	0.86	2.25 ± 0.28
	HD C-S-H	13.65	8.64	73.92	0.58	0.78	0.43	0.35	0.81	0.84	1.58 ± 0.22
	LD C-S-H	9.97	16.68	69.47	0.58	0.79	0.46	0.34	0.84	0.87	0.60 ± 0.23
	Sand	–	36.94	63.06	–	–	–	–	–	–	–
	Clinker	26.12	4.28	62.83	1.15	1.69	1.54	–	1.27	1.12	6.10 ± 0.18
	CH	18.16	0.83	77.01	0.60	0.82	0.45	0.37	0.86	0.90	–
MH	UHD C-S-H	–	–	–	–	–	–	–	–	–	–
	HD C-S-H	11.46	10.19	74.49	0.55	0.80	0.45	0.33	0.88	0.85	1.12 ± 0.32
	LD C-S-H	9.01	17.38	69.64	0.56	0.82	0.44	0.37	0.91	0.87	0.52 ± 0.19
	Sand	–	35.78	64.22	–	–	–	–	–	–	–
	Clinker	31.42	5.22	56.51	1.31	1.57	1.54	–	1.34	1.09	6.02 ± 0.29
	CH	18.45	0.76	76.74	0.58	0.83	0.48	0.36	0.92	0.88	–

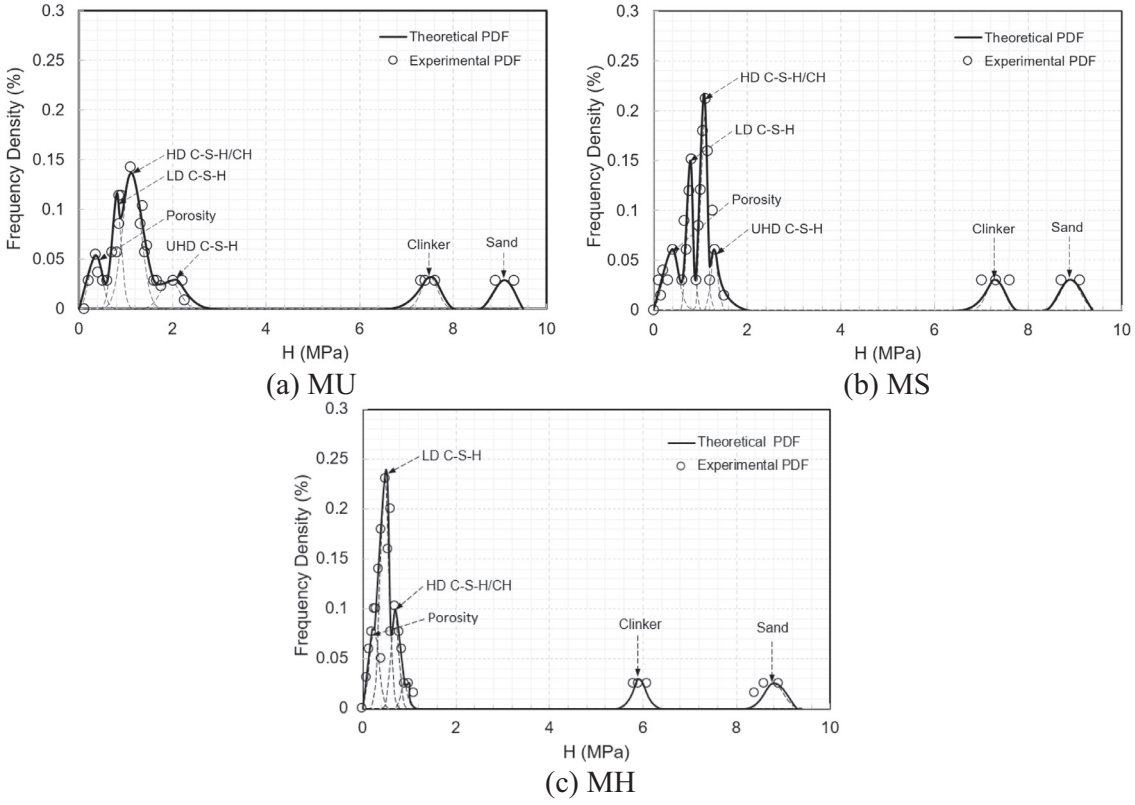

Fig. 11. Experimental frequency plots and the theoretical PDF for H of indents in FMZ of MU, MH, and MH at loading rate 1 mN/s.

a theoretical model for the materials with $E/\sigma_y < 10^3$ (where σ_y is a compressive yield stress and calculated according to Eq. (13)) to solve the pressure-sensitive indentation problem by using the following analogy between the indentation deformation and pressurized-spherical-hole model, as illustrated in Fig. 15.

$$\sigma_y = \frac{H}{C} \tag{13}$$

where H is given by Eq. (1) and C is a constraint factor considered to reflect the degree of confinement effect provided by material surrounding an indenter tip [59]. The C was approximately equal to 3.0 for materials with high values of the elastic modulus to compressive yield stress ratio [44,59–63].

Fig. 15a shows an ideal elastic–plastic yield criterion with pressure hardening for uniaxial compression at various confining pressures (σ). Fig. 15b and c show a schematic of stress in a plastic zone under a flat rigid die with a pressure-hardening effect and the volume of depression under an indenter, respectively. The relationship between σ and σ_y is given by Eq. (14) [57]

$$\sigma_y = \sigma_0 + \alpha\,\sigma \tag{14}$$

where σ_0 and α are the compressive yield stress at zero pressure and the coefficient of pressure hardening, respectively. The α was

Table 5
Deconvolution results of the FMZs of MU, MS, and MH matrix.

Matrix	Microstructures	1 (mN/s)			8 (mN/s)			Mean
		H $\mu_j \pm s_j$ (GPa)	E $\mu_j \pm s_j$ (GPa)	f_j (%)	H $\mu_j \pm s_j$ (GPa)	E $\mu_j \pm s_j$ (GPa)	f_j (%)	f_j (%)
MU	UHD C-S-H	1.92 ± 0.23	41.03 ± 3.61	11.12	2.99 ± 0.13	56.57 ± 7.80	10.65	10.89
	HD C-S-H	1.25 ± 0.13	32.00 ± 2.82	25.00	1.90 ± 0.40	43.07 ± 10.70	26.31	25.66
	LD C-S-H	0.82 ± 0.19	26.49 ± 5.15	33.33	1.19 ± 0.17	34.65 ± 3.03	32.12	32.73
	CH	1.04 ± 0.11	29.71 ± 1.92	10.71	1.51 ± 0.05	39.26 ± 1.39	10.01	10.36
	Clinker	7.48 ± 0.10	116.34 ± 1.11	10.00	11.75 ± 0.09	164.44 ± 1.55	10.24	10.12
	Sand	9.11 ± 0.21	96.48 ± 2.43	5.88	14.68 ± 0.86	140.79 ± 2.20	6.01	5.95
	Porosity	0.32 ± 0.09	8.71 ± 0.26	3.96	0.58 ± 0.12	9.31 ± 0.33	4.66	4.31
MS	UHD C-S-H	1.36 ± 0.00	33.28 ± 0.00	3.03	2.10 ± 0.00	48.38 ± 0.00	3.21	3.12
	HD C-S-H	1.15 ± 0.09	31.47 ± 2.15	27.27	1.74 ± 0.16	42.73 ± 3.28	26.95	27.11
	LD C-S-H	0.76 ± 0.18	26.61 ± 3.37	36.37	0.90 ± 0.15	30.74 ± 5.16	37.01	36.69
	CH	1.09 ± 0.03	31.87 ± 1.53	10.34	1.36 ± 0.03	36.63 ± 0.57	9.88	10.11
	Clinker	7.35 ± 0.23	113.01 ± 1.12	9.09	11.47 ± 0.44	157.48 ± 0.51	9.21	9.15
	Sand	8.95 ± 0.17	87.78 ± 0.50	6.06	14.50 ± 0.54	127.16 ± 1.51	5.87	5.97
	Porosity	0.24 ± 0.08	6.51 ± 0.36	7.84	0.45 ± 0.10	8.37 ± 0.16	7.87	7.86
MH	UHD C-S-H	–	–	–	–	–	–	–
	HD C-S-H	0.82 ± 0.08	25.57 ± 3.16	15.00	1.13 ± 0.08	28.23 ± 3.65	14.96	14.98
	LD C-S-H	0.52 ± 0.07	22.89 ± 5.82	47.50	0.60 ± 0.10	23.13 ± 4.86	47.77	47.64
	CH	0.92 ± 0.16	34.09 ± 1.83	10.00	1.12 ± 0.22	36.60 ± 0.21	9.82	9.91
	Clinker	5.99 ± 0.11	118.65 ± 1.59	7.50	9.21 ± 0.05	132.61 ± 2.22	7.24	7.37
	Sand	8.81 ± 0.14	97.57 ± 1.16	5.00	14.33 ± 0.45	118.16 ± 4.42	5.22	5.11
	Porosity	0.21 ± 0.03	5.62 ± 0.28	15.00	0.30 ± 0.18	7.11 ± 0.34	14.99	15.00

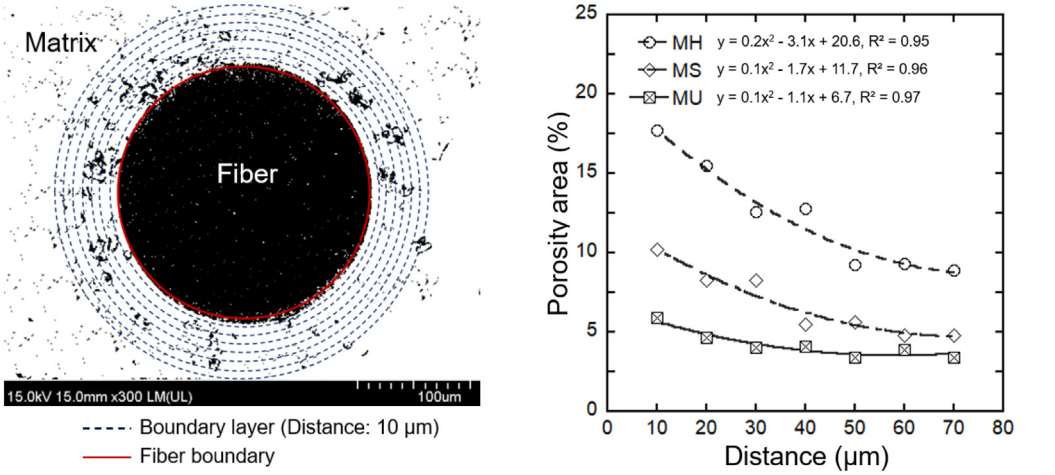

(a) Boundary layers in FMZ (b) Percentage of porosity area with distance from fiber surface

Fig. 12. Calculation of the porosity area in FMZ corresponding to MH, MS, and MU.

used to represent the material sensitivity to pressure hardening. Thus, the higher value of α produced higher material sensitivity to pressure-hardening [32,44]. The α was calculated from Eq. (15) [57].

$$H_0 = (3 + 2\alpha)\,\sigma_0 \tag{15}$$

where H_0 is given in Eq. (7). The σ_0 are determined by fitting the curve between σ_y and $\dot{P}$ in Eq.(16) [32,44].

$$\sigma_y = \sigma_0 + \beta\dot{P} \tag{16}$$

The σ_y of MU, MS, and MH at loading rate ($\dot{P}$) of 1 mN/s was obtained as 0.73, 0.68, and 0.53 GPa, respectively by using Eq. (13) while it was 1.28, 1.02, and 0.77 GPa, respectively at the loading rate of 8 mN/s. β is a constant factor depending on the properties of materials.

Fig. 16 shows the relationship between σ_y and $\dot{P}$ of MU, MS, and MH, respectively. The σ_0 was 0.65, 0.63, and 0.5 GPa for MU, MS, and MH, respectively.

The value of α of MU, MS, and MH was 2.27, 1.38, and 1.25, respectively. The α of the MU matrix was the highest whereas that of the MH matrix was the lowest. Table 6 summarizes the α of the LD C-S-H, HD C-S-H, UHD C-S-H, CH, clinker, and sand. The α of sand was the highest among the microstructures in FMZ of the matrices. Besides, the α of UHD C-S-H was higher than that of HD and LD C-S-H. The α of UHD C-S-H was between 1.31 and 1.36, while that in HD and LD C-S-H was varied from 0.87 to 1.25 and 0.21 to 1.10, respectively. It was clear that both UHD and HD C-S-H were more sensitive to pressure hardening than LD C-S-H.

Eq. (17) presents an analytical equation, for n as a function of α, which was obtained from Eqs. (5), (9), and (10). Fig. 17 presents the

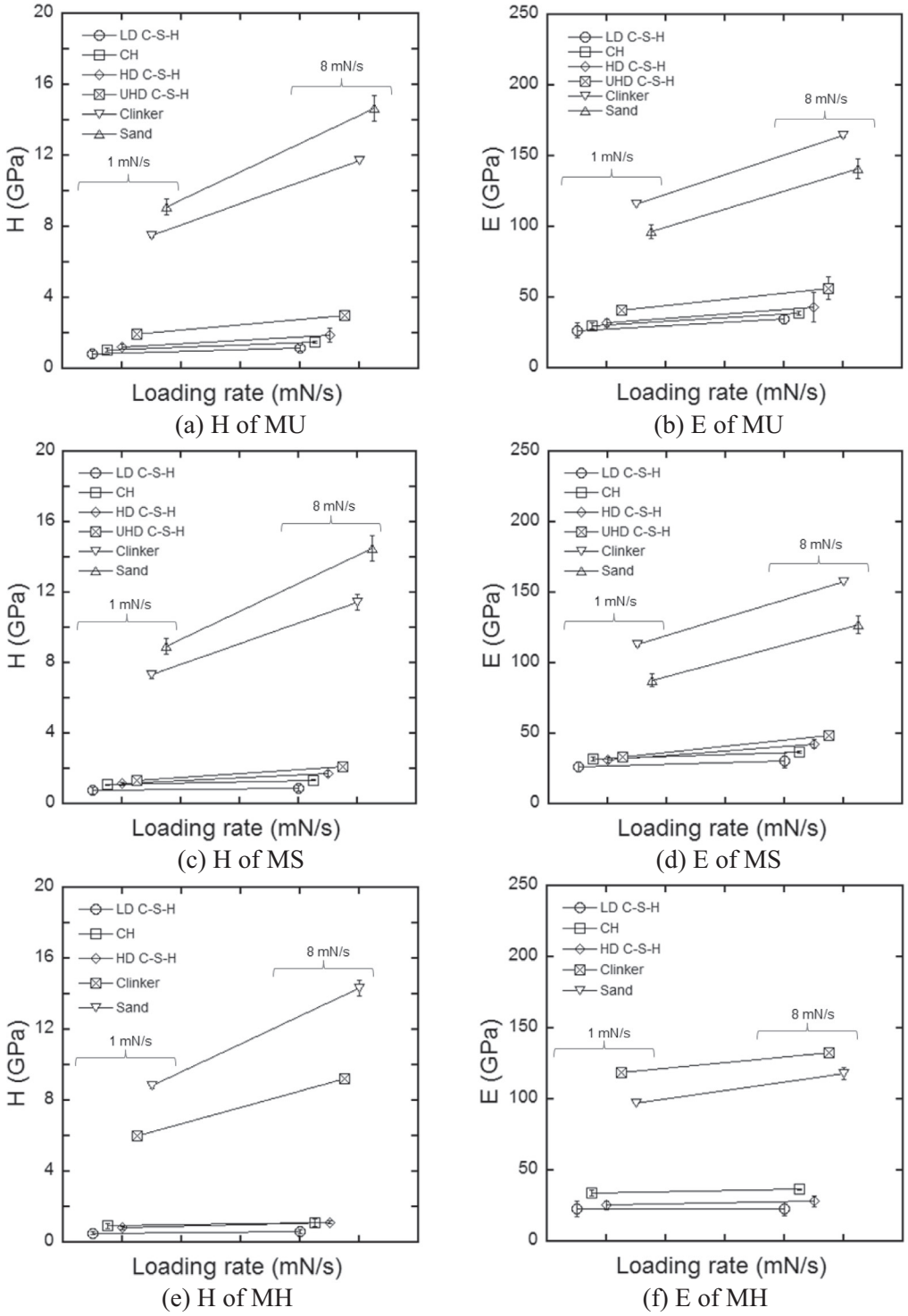

Fig. 13. Loading rate effects on Hardness and Young's modulus of microstructures.

correlation between strain rate sensitivity (n) and coefficient of pressure hardening (α).

$$n = \frac{\log\left[(\sigma_0 + \alpha\sigma_2)/(\sigma_0 + \alpha\sigma_1)\right]}{\log\left(\dot{\varepsilon}_2/\dot{\varepsilon}_1\right)} \quad (17)$$

where σ_1 and σ_2 were confining pressures at low and high strain rates, as calculated from Eq. (14) while ε_1 and ε_2 were the low and high strain rates.

As the coefficient of pressure hardening (α) of microstructures or matrices increased, the strain rate sensitivity (n) clearly increased, as shown in Fig. 17. Thus, the MU matrix with higher pressure hardening sensitivity (α) produced higher loading rate sensitivity (n) in comparison with other matrices. In addition, the UHD and HD C-S-H with higher pressure hardening sensitivity generated higher strain rate sensitivity than the LD C-S-H.

Fig. 18 shows the rate sensitivity of the equivalent bond strength and nanoindentation hardness in FMZ of matrices. The

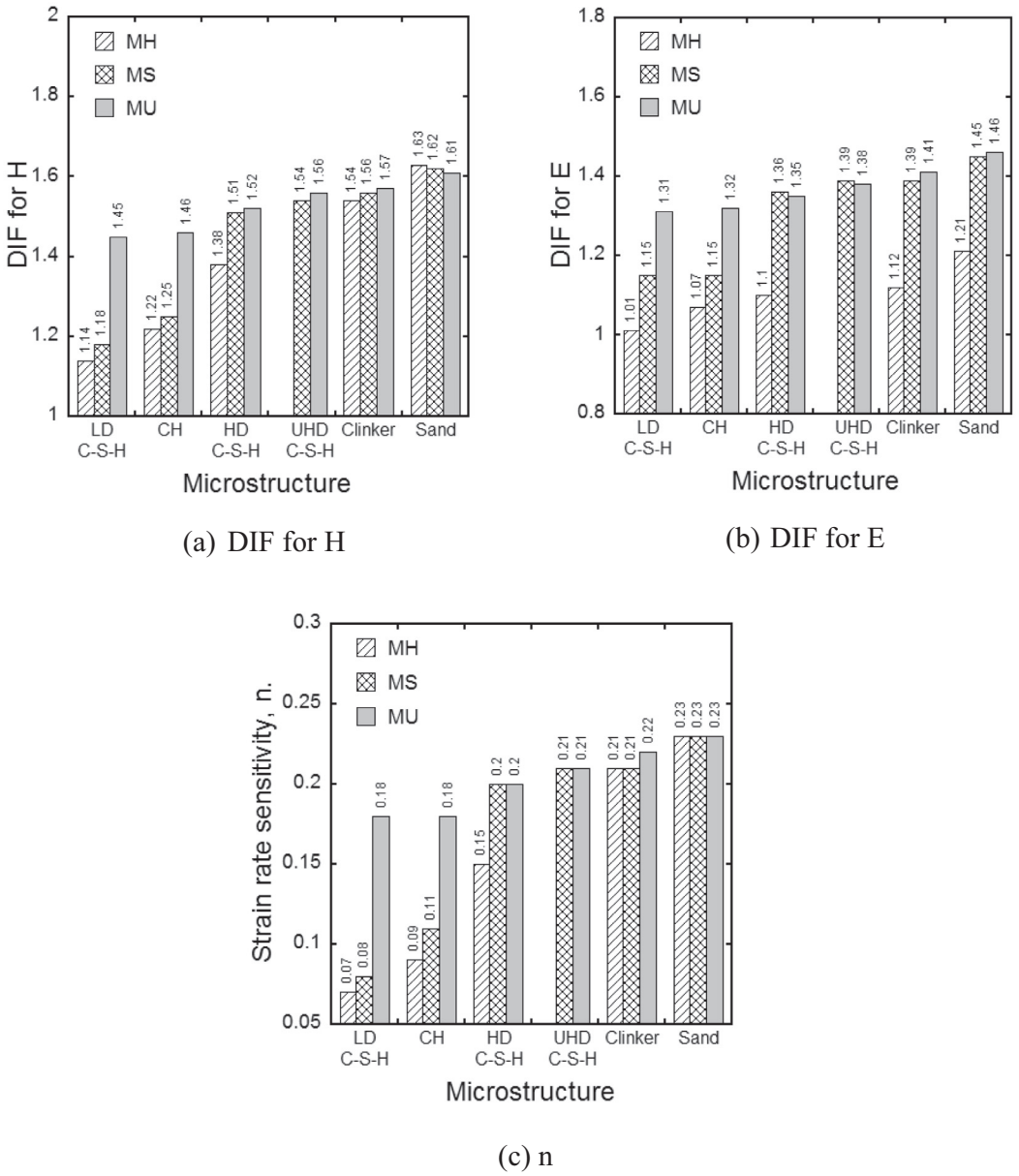

Fig. 14. DIFs for H and E, and strain rate sensitivity (n) corresponding to different microstructures in FMZ of MH, MS, and MU matrix.

trend of the loading or strain rate sensitivity of FMZ in this study was consistent with the pullout rate sensitivity reported in [10,11] for the same matrices and fibers. Park et al [10,11] reported that the pullout rate sensitivity of smooth steel fiber embedded in the MU was the highest in comparison with that of MS and MH matrices. The loading or strain rate sensitivity in cement based matrix was dependent upon the properties of interfacial transition zone between matrix and fiber. Based on the observation of this study for FMZ at nanoscale, the experimental frequency of C-S-H in MU (69.28%) was higher than that in MS (66.92%) and MH (62.62%), as provided in Table 5. Furthermore, the percentage of UHD and HD C-S-H in the FMZ of the MU matrix (with the highest strain/loading rate sensitivity) was the highest value (36.55%) whereas that of the MH matrix was the lowest one (14.98%), as summarised in Table 5. Consequently, the MU matrix was more sensitive to the loading or strain rates than the MS and MH matrices.

5. Conclusions

In this study, we investigated the effect of loading rate on the fiber–matrix zone (FMZ) between smooth steel fiber and cement based matrix. The nanoindentation (NI) test was carried out with the loading rates from 1 to 8 mN/s. Scanning electron microscopic (SEM) and Energy-dispersive X-ray spectroscopy (EDS) analyses were also conducted to observe the surface morphology of FMZ areas and identify the chemical characterization of indented points. Based on the experimental results, following conclusions could be obtained, even though the investigated loading rate was limited from static to seismic rate.

- As the loading rate increased from 1 to 8 mN/s, the maximum indentation depth (h_{max}), contact depth (h_c), and contact area (A_c) clearly decreased.

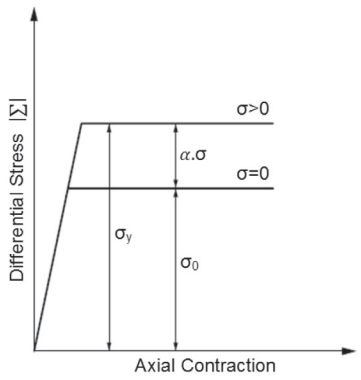

(a) Stress-strain curve of ideal elastic-plastic solid with pressure hardening

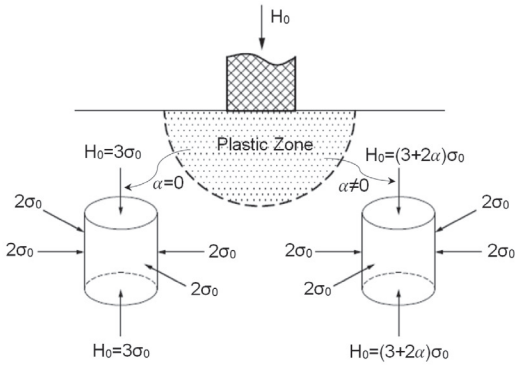

(b) Schematic of stress in a plastic zone under flat rigid die with pressure-hardening effect

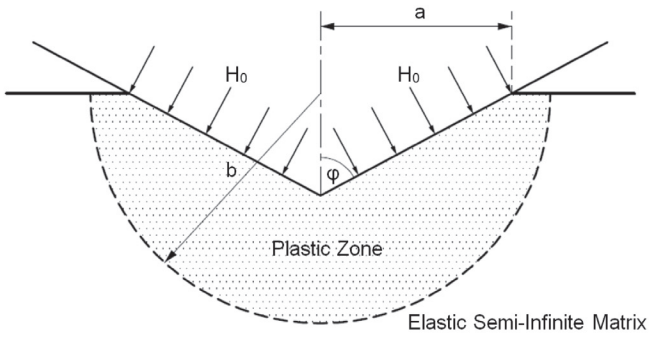

(c) Pyramidal indentation into half-space

Fig. 15. An ideal elastic–plastic yield criterion with pressure-hardening [57].

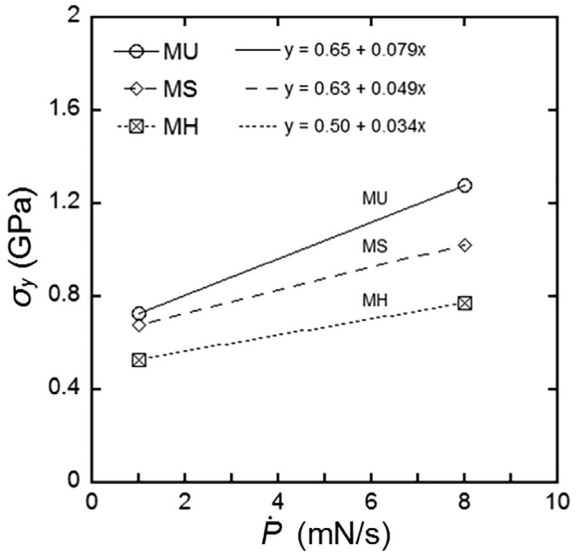

Fig. 16. The relationship between compressive yield stress and loading rate.

- In addition, the MU, among the three matrices including MU, MS, and MH, generated the highest rate sensitivity for the *H* of FMZ whereas MH did the lowest one. The dynamic increase factor (*DIF*) was 1.75 and 1.46 for the H of MU and MH matrices, respectively.
- The higher *DIF* for *H* of MU would be based on the higher content of UHD C-S-H (11.12%) and HD C-S-H (25.00%), highly sensitive to the loading rates, in MU than other matrices including MS and MH.
- Among the microstructures (including LD C-S-H, HD C-S-H, UHD C-S-H, CH, clinker, and sand) in FMZ, sand obviously produced the highest rate sensitivity (*DIF* of *H* = 1.61 for MU matrix) of FMZ whereas LD C-S-H did the lowest one (*DIF* of *H* = 1.45 for MU matrix).
- The C-S-H with higher Ca/Si ratio generated higher rate sensitivity: the *DIF* for the *H* was 1.56, 1.52, and 1.45 for UHD, HD, and LD C-S-H, while the Ca/Si ratio of C-S-H was 2.36, 1.70, and 0.72 for UHD, HD, and LD C-S-H in MU, respectively.

The test results of this study suggested that the loading or strain rate sensitivity of HPFRCC matrices would be improved by increasing the C-S-H with higher Ca/Si ratio at the FMZ surrounding the

Table 6
The parameter characteristics of the microstructures in FMZs.

Matrix	*FMZ*	n	H_0 (GPa)	σ_y (GPa)		σ_0 (GPa)	α
				1 (mN/s)	8 (mN/s)		
MU	UHD C-S-H	0.21	3.63	0.69	1.07	0.64	1.36
	HD C-S-H	0.20	2.28	0.45	0.68	0.42	1.24
	LD C-S-H	0.18	1.40	0.29	0.43	0.27	1.10
	CH	0.18	1.78	0.37	0.54	0.35	1.07
	Clinker	0.22	14.34	2.67	4.20	2.45	1.43
	Sand	0.23	18.11	3.25	5.24	2.97	1.55
MS	UHD C-S-H	0.21	2.54	0.49	0.75	0.45	1.31
	HD C-S-H	0.20	2.09	0.41	0.62	0.38	1.25
	LD C-S-H	0.08	0.97	0.27	0.32	0.26	0.34
	CH	0.11	1.50	0.39	0.49	0.38	0.49
	Clinker	0.21	13.95	2.63	4.10	2.42	1.38
	Sand	0.23	17.93	3.20	5.18	2.92	1.57
MH	UHD C-S-H	–	–	–	–	–	–
	HD C-S-H	0.15	1.30	0.29	0.40	0.27	0.87
	LD C-S-H	0.07	0.64	0.19	0.21	0.19	0.21
	CH	0.09	1.22	0.33	0.40	0.32	0.41
	Clinker	0.21	11.13	2.14	3.29	1.98	1.31
	Sand	0.23	17.75	3.15	5.12	2.87	1.59

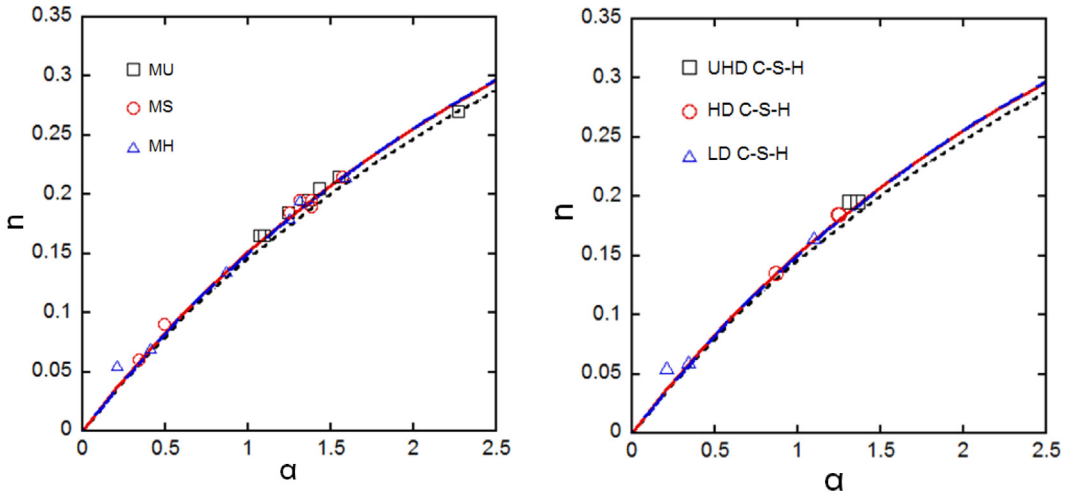

(a) Effect of different matrix (b) Effect of different C-S-H

Fig. 17. Correlation between n and α.

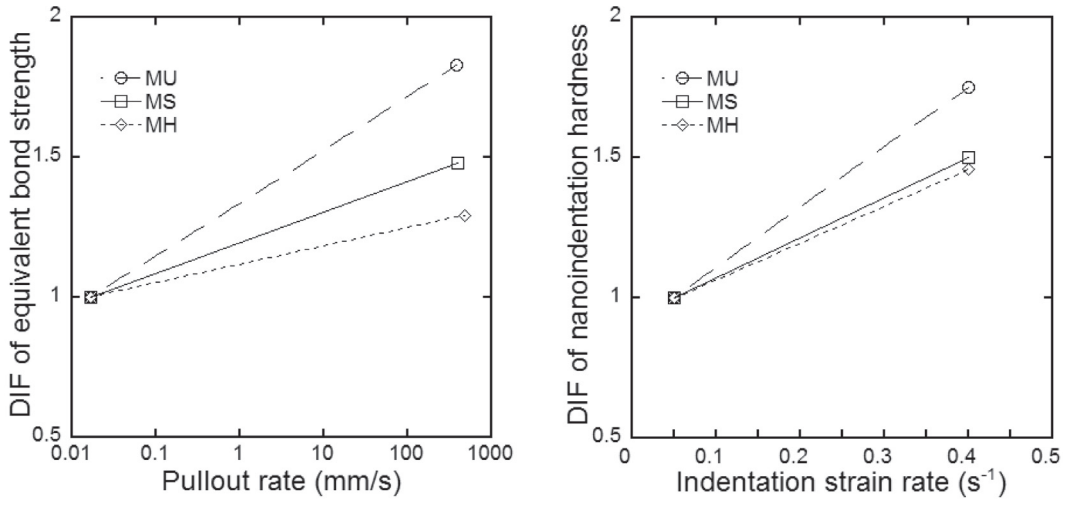

(a) DIF of equivalent bond strength [11] (b) DIF of H

Fig. 18. The rate sensitivity of equivalent bond strength and nanoindentation hardness of different matrices.

fibers. The potential materials such as nano silica, nano calcium carbonate, and nano calcium oxide can be added to the MU matrix in order to further increase the UHD and HD C-S-H at the FMZ and consequently enhance the loading or strain rate sensitivity of the matrix.

CRediT authorship contribution statement

Van Phi Dang: Investigation, Writing - original draft. **Huy Viet Le:** Writing - review & editing. **Dong Joo Kim:** Methodology, Supervision, Writing - review & editing.

Declaration of Competing Interest

The authors declare that they have no known competing financial interests or personal relationships that could have appeared to influence the work reported in this paper.

Acknowledgments

This research was supported by the Basic Science Research Program through the National Research Foundation of Korea (NRF) funded by the Ministry of Education (NRF-2019R1F1A106006612).

References

[1] D.J. Kim, S. El-Tawil, A.E. Naaman, Correlation between single fiber pullout and tensile response of FRC composites with high strength steel fibers, HPFRCC5, Mainz, Ger. (2007) 67–76.
[2] A.E. Naaman, H.W. Reinhardt, Proposed classification of HPFRC composites based on their tensile response, Mater. Struct. Constr. 39 (2006) 547–555, https://doi.org/10.1617/s11527-006-9103-2.
[3] D.J. Kim, S. El-Tawil, A.E. Naaman, Rate-dependent tensile behavior of high performance fiber reinforced cementitious composites, Mater. Struct. Constr. 42 (2009) 399–414, https://doi.org/10.1617/s11527-008-9390-x.
[4] K.S. Douglas, Sarah L. Billington, Rate dependence in high-performance fiber-reinforced cement-based composites for seismic applications, Proceedings, HPFRCC- 2005 Int. Work. Honolulu, Hawaii, USA. (2005) 17–25. https://doi.org/10.1617/2912143942.003.
[5] M. Maalej, S.T. Quek, J. Zhang, Behavior of hybrid-fiber engineered cementitious composites subjected to dynamic tensile loading and projectile impact, J. Mater. Civ. Eng. 17 (2005) 143–152, https://doi.org/10.1061/(ASCE)0899-1561(2005)17:2(143).
[6] T.K. Tran, D.J. Kim, High strain rate effects on direct tensile behavior of high performance fiber reinforced cementitious composites, Cem. Concr. Compos. 45 (2014) 186–200, https://doi.org/10.1016/j.cemconcomp.2013.10.005.
[7] U.N. Gokoz, A.E. Naaman, Effect of strain-rate on the pull-out behaviour of fibres in mortar, Int. J. Cem. Compos. Light. Concr. 3 (1981) 187–202, https://doi.org/10.1016/0262-5075(81)90051-8.
[8] D.J. Kim, S. El-Tawil, A.E. Naaman, Loading rate effect on pullout behavior of deformed steel fibers, ACI Mater. J. 105 (2008) 576–584, https://doi.org/10.14359/20199.
[9] Y.S. Tai, S. El-Tawil, High loading-rate pullout behavior of inclined deformed steel fibers embedded in ultra-high performance concrete, Constr. Build. Mater. 148 (2017) 204–218, https://doi.org/10.1016/j.conbuildmat.2017.05.018.
[10] J.K. Park, S.H. Park, D.J. Kim, Effect of matrix shrinkage on rate sensitivity of the pullout response of smooth steel fibers in ultra-high-performance concrete, Cem. Concr. Compos. 94 (2018) 226–237, https://doi.org/10.1016/j.cemconcomp.2018.09.014.
[11] J.K. Park, T.T. Ngo, D.J. Kim, Interfacial bond characteristics of steel fibers embedded in cementitious composites at high rates, Cem. Concr. Res. 123 (2019), https://doi.org/10.1016/j.cemconres.2019.105802 105802.
[12] G.L. Golewski, The influence of microcrack width on the mechanical parameters in concrete with the addition of fly ash: Consideration of technological and ecological benefits, Constr. Build. Mater. 197 (2019) 849–861, https://doi.org/10.1016/j.conbuildmat.2018.08.157.
[13] S.H. Kang, J.J. Kim, D.J. Kim, Y.S. Chung, Effect of sand grain size and sand-to-cement ratio on the interfacial bond strength of steel fibers embedded in mortars, Constr. Build. Mater. 47 (2013) 1421–1430, https://doi.org/10.1016/j.conbuildmat.2013.06.064.
[14] S.H. Park, G.S. Ryu, K.T. Koh, D.J. Kim, Effect of shrinkage reducing agent on pullout resistance of high-strength steel fibers embedded in ultra-high-performance concrete, Cem. Concr. Compos. 49 (2014) 59–69, https://doi.org/10.1016/j.cemconcomp.2013.12.012.
[15] M. Xu, B. Hallinan, K. Wille, Effect of loading rates on pullout behavior of high strength steel fibers embedded in ultra-high performance concrete, Cem. Concr. Compos. 70 (2016) 98–109, https://doi.org/10.1016/j.cemconcomp.2016.03.014.
[16] J.J. Kim, D.J. Kim, S.T. Kang, J.H. Lee, Influence of sand to coarse aggregate ratio on the interfacial bond strength of steel fibers in concrete for nuclear power plant, Nucl. Eng. Des. 252 (2012) 1–10, https://doi.org/10.1016/j.nucengdes.2012.07.004.
[17] L. Xu, F. Deng, Y. Chi, Nano-mechanical behavior of the interfacial transition zone between steel-polypropylene fiber and cement paste, Constr. Build. Mater. 145 (2017) 619–638, https://doi.org/10.1016/j.conbuildmat.2017.04.035.
[18] T. Akçaoğlu, M. Tokyay, T. Çelik, Assessing the ITZ microcracking via scanning electron microscope and its effect on the failure behavior of concrete, Cem. Concr. Res. 35 (2005) 358–363, https://doi.org/10.1016/j.cemconres.2004.05.042.
[19] S. Diamond, J. Huang, The ITZ in concrete – a different view based on image analysis and SEM observations, Cem. Concr. Compos. 23 (2001) 179–188, https://doi.org/10.1016/S0958-9465(00)00065-2.
[20] L. Gatty, S. Bonnamy, A. Feylessoufi, C. Clinard, P. Richard, H. Van Damme, A transmission electron microscopy study of interfaces and matrix homogeneity in ultra high performance cement based materials, J. Mater. Sci. 36 (2001) 4013–4026, https://doi.org/10.1023/A:1017938725748.
[21] K.L. Scrivener, A.K. Crumbie, P. Laugesen, The interfacial transition zone (ITZ) between cement paste and aggregate in concrete, Interface Sci. 12 (2004) 411–421, https://doi.org/10.1023/B:INTS.0000042339.92990.4c.
[22] K.L. Scrivener, Backscattered electron imaging of cementitious microstructures: Understanding and quantification, Cem. Concr. Compos. 26 (2004) 935–945, https://doi.org/10.1016/j.cemconcomp.2004.02.029.
[23] Y.W. Chan, S.H. Chu, Effect of silica fume on steel fiber bond characteristics in reactive powder concrete, Cem. Concr. Res. 34 (2004) 1167–1172, https://doi.org/10.1016/j.cemconres.2003.12.023.
[24] A. Elsharief, M.D. Cohen, J. Olek, Influence of aggregate size, water cement ratio and age on the microstructure of the interfacial transition zone, Cem. Concr. Res. 33 (2003) 1837–1849, https://doi.org/10.1016/S0008-8846(03)00205-9.
[25] V.C. Li, H. Stang, Interface property characterization and strengthening mechanisms in fiber reinforced cement based composites, Adv. Cem. Bas. Mat. 6 (1997) 1–20.
[26] G.L. Golewski, A novel specific requirements for materials used in reinforced concrete composites subjected to dynamic loads, Compos. Struct. 223 (2019), https://doi.org/10.1016/j.compstruct.2019.110939 110939.
[27] G.L. Golewski, Energy savings associated with the use of fly ash and nanoadditives in the cement composition, Energies 13 (2020), https://doi.org/10.3390/en13092184.
[28] V. Zanjani Zadeh, C.P. Bobko, Nano-mechanical properties of internally cured kenaf fiber reinforced concrete using nanoindentation, Cem. Concr. Compos. 52 (2014) 9–17, https://doi.org/10.1016/j.cemconcomp.2014.04.002.
[29] S. Zhao, W. Sun, Nano-mechanical behavior of a green ultra-high performance concrete, Constr. Build. Mater. 63 (2014) 150–160, https://doi.org/10.1016/j.conbuildmat.2014.04.029.
[30] M. Vandamme, F.J. Ulm, P. Fonollosa, Nanogranular packing of C-S-H at substochiometric conditions, Cem. Concr. Res. 40 (2010) 14–26, https://doi.org/10.1016/j.cemconres.2009.09.017.
[31] L. Sorelli, G. Constantinides, F.J. Ulm, F. Toutlemonde, The nano-mechanical signature of ultra high performance concrete by statistical nanoindentation techniques, Cem. Concr. Res. 38 (2008) 1447–1456, https://doi.org/10.1016/j.cemconres.2008.09.002.
[32] X. Shi, Z. He, S. Long, Y. Peng, D. Li, S. Jiang, Loading rate effect on the mechanical behavior of brittle longmaxi shale in nanoindentation, Int. J. Hydrogen Energy. 44 (2019) 6481–6490, https://doi.org/10.1016/j.ijhydene.2019.01.028.
[33] X. Li, L. Jiang, J. Li, I. Mohagheghian, J.P. Dear, L. Li, Y. Yan, Elastic-plastic deformation in ion-exchanged aluminosilicate glass by loading rate dependent nanoindentation, J. Non. Cryst. Solids. 491 (2018) 79–88, https://doi.org/10.1016/j.jnoncrysol.2018.04.003.
[34] M. Bhattacharya, A. Dey, A.K. Mukhopadhyay, Influence of loading rate on nanohardness of sapphire, Ceram. Int. 42 (2016) 13378–13386, https://doi.org/10.1016/j.ceramint.2016.05.091.
[35] T. Burgess, K.J. Laws, M. Ferry, Effect of loading rate on the serrated flow of a bulk metallic glass during nanoindentation, Acta Mater. 56 (2008) 4829–4835, https://doi.org/10.1016/j.actamat.2008.05.039.
[36] N.V. Nguyen, T.H. Pham, S.E. Kim, Microstructure and strain rate sensitivity behavior of SM490 structural steel weld zone investigated using indentation, Constr. Build. Mater. 206 (2019) 410–418, https://doi.org/10.1016/j.conbuildmat.2019.02.013.
[37] S. Xu, Y. Feng, J. Liu, Q. Zeng, Micro indentation fracture of cement paste assessed by energy-based method: The method improvement and affecting factors, Constr. Build. Mater. 231 (2020), https://doi.org/10.1016/j.conbuildmat.2019.117136 117136.
[38] A.C. Barone, M. Anglada, J. Alcala, The influence of plastic hardening on surface deformation modes around Vickers and Spherical indents, Acta Mater. 48 (2000) 3451–3464.

[39] W.C. Oliver, G.M. Pharr, An improved technique for determining hardness and elastic modulus using load and displacement sensing indentation experiments, J. Mater. Res., 6 (7) (1992) 1564–1583, https://doi.org/10.1177/003591571901200704.
[40] N.V. Nguyen, T.H. Pham, S.E. Kim, Characterization of strain rate effects on the plastic properties of structural steel using nanoindentation, Constr. Build. Mater. 163 (2018) 305–314, https://doi.org/10.1016/j.conbuildmat.2017.12.122.
[41] K. Durst, V. Maier, Dynamic nanoindentation testing for studying thermally activated processes from single to nanocrystalline metals, Curr. Opin. Solid State Mater. Sci. 19 (2015) 340–353, https://doi.org/10.1016/j.cossms.2015.02.001.
[42] N.V. Nguyen, T.H. Pham, S.E. Kim, Strain rate-dependent behaviors of mechanical properties of structural steel investigated using indentation and finite element analysis, Mech. Mater. 137 (2019), https://doi.org/10.1016/j.mechmat.2019.103089 103089.
[43] Y.C. Lu, G.P. Tandon, S. Putthanarat, G.A. Schoeppner, Nanoindentation strain rate sensitivity of thermo-oxidized PMR-15 polyimide, J. Mater. Sci. 44 (2009) 2119–2127, https://doi.org/10.1007/s10853-009-3311-4.
[44] A.R. Alao, L. Yin, Loading rate effect on the mechanical behavior of zirconia in nanoindentation, Mater. Sci. Eng. A. 619 (2014) 247–255, https://doi.org/10.1016/j.msea.2014.09.101.
[45] S. Liang, Y. Wei, X. Gao, Strain-rate sensitivity of cement paste by microindentation continuous stiffness measurement: implication to isotache approach for creep modeling, Cem. Concr. Res. 100 (2017) 84–95, https://doi.org/10.1016/j.cemconres.2017.05.023.
[46] C. Hu, Z. Li, A review on the mechanical properties of cement-based materials measured by nanoindentation, Constr. Build. Mater. 90 (2015) 80–90, https://doi.org/10.1016/j.conbuildmat.2015.05.008.
[47] M. Miller, C. Bobko, M. Vandamme, F.J. Ulm, Surface roughness criteria for cement paste nanoindentation, Cem. Concr. Res. 38 (2008) 467–476, https://doi.org/10.1016/j.cemconres.2007.11.014.
[48] W. Ashraf, N. Tian, Nanoindentation assisted investigation on the viscoelastic behavior of carbonated cementitious matrix: influence of loading function, Constr. Build. Mater. 127 (2016) 904–917, https://doi.org/10.1016/j.conbuildmat.2016.10.021.
[49] R.J. Anton, G. Subhash, Dynamic Vickers indentation of brittle materials, Wear 239 (2000) 27–35, https://doi.org/10.1016/S0043-1648(99)00364-6.
[50] M.A. Klecka, G. Subhash, Rate-dependent indentation response of structural ceramics, J. Am. Ceram. Soc. 93 (2010) 2377–2383, https://doi.org/10.1111/j.1551-2916.2010.03729.x.
[51] M. Bhattacharya, R. Chakraborty, A. Dey, A.K. Mandal, A.K. Mukhopadhyay, Improvement in nanoscale contact resistance of alumina, Appl. Phys. A Mater. Sci. Process. 107 (2012) 783–788, https://doi.org/10.1007/s00339-012-6888-4.
[52] G. Constantinides, F.J. Ulm, The nanogranular nature of C-S-H, J. Mech. Phys. Solids. 55 (2007) 64–90, https://doi.org/10.1016/j.jmps.2006.06.003.
[53] C. Hu, Y. Han, Y. Gao, Y. Zhang, Z. Li, Property investigation of calcium-silicate-hydrate (C-S-H) gel in cementitious composites, Mater. Charact. 95 (2014) 129–139, https://doi.org/10.1016/j.matchar.2014.06.012.
[54] C. Hu, Microstructure and mechanical properties of fly ash blended cement pastes, Constr. Build. Mater. 73 (2014) 618–625, https://doi.org/10.1016/j.conbuildmat.2014.10.009.
[55] W. Ashraf, J. Olek, N. Tian, Multiscale characterization of carbonated wollastonite paste and application of homogenization schemes to predict its effective elastic modulus, Cem. Concr. Compos. 72 (2016) 284–298, https://doi.org/10.1016/j.cemconcomp.2016.05.023.
[56] D. Wang, C. Shi, Z. Wu, J. Xiao, Z. Huang, Z. Fang, A review on ultra high performance concrete: Part II. Hydration, microstructure and properties, Constr. Build. Mater. 96 (2015) 368–377, https://doi.org/10.1016/j.conbuildmat.2015.08.095.
[57] I. Chen, Implications of transformation plasticity in ZrO2-Containing, Sci. Technol. 4 (1986).
[58] I.W. Chen, P.E.R. Morel, Implications of transformation plasticity in ZrO2-Containing ceramics: I, shear and dilatation effects, J. Am. Ceram. Soc. 69 (1986) 181–189, https://doi.org/10.1111/j.1151-2916.1986.tb07403.x.
[59] D. Katsuki, M. Gutierrez, Nanoindentation approach characterizing strain rate sensitivity of compressive response of asphalt concrete, Acta Geotech. 9 (2014) 887–901, https://doi.org/10.1007/s11440-013-0269-9.
[60] A. Dey, R. Chakraborty, A.K. Mukhopadhyay, Nanoindentation of soda lime-silica glass: Effect of loading rate, Int. J. Appl. Glas. Sci. 2 (2011) 144–155, https://doi.org/10.1111/j.2041-1294.2011.00046.x.
[61] J. Fu, S. Kamali-Bernard, F. Bernard, M. Cornen, Comparison of mechanical properties of C-S-H and portlandite between nano-indentation experiments and a modeling approach using various simulation techniques, Compos. Part B Eng. 151 (2018) 127–138, https://doi.org/10.1016/j.compositesb.2018.05.043.
[62] B.R. Bodapati, P. Sudharshan Phani, P.P. Bhattacharjee, G. Sundararajan, On the constraint factor and Tabor coefficient pertinent to spherical indentation, Trans. Indian Inst. Met. 71 (2018) 2893–2901, https://doi.org/10.1007/s12666-018-1388-7.
[63] R. Solids, P. Chemistry, S.G. Taylor, A simple theory of static and dynamic hardness, Proc. R. Soc. London. Ser. A. Math. Phys. Sci. 192 (1948) 247–274, https://doi.org/10.1098/rspa.1948.0008.